NASA TECHNICAL NOTE

NASA TN D-3218

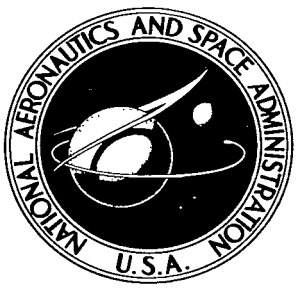

A THEORETICAL AND EXPERIMENTAL STUDY OF HYPERSONIC FLOW OVER FLARED BODIES AT INCIDENCE

by John V. Rakich and Gene P. Menees

Ames Research Center
Moffett Field, Calif.

NATIONAL AERONAUTICS AND SPACE ADMINISTRATION • WASHINGTON, D. C. • JANUARY 1966

NASA TN D-3218

A THEORETICAL AND EXPERIMENTAL STUDY OF HYPERSONIC FLOW OVER FLARED BODIES AT INCIDENCE

By John V. Rakich and Gene P. Menees

Ames Research Center
Moffett Field, Calif.

NATIONAL AERONAUTICS AND SPACE ADMINISTRATION

For sale by the Clearinghouse for Federal Scientific and Technical Information
Springfield, Virginia 22151 – Price $2.00

A THEORETICAL AND EXPERIMENTAL STUDY OF HYPERSONIC FLOW OVER FLARED BODIES AT INCIDENCE

By John V. Rakich and Gene P. Menees
Ames Research Center

SUMMARY

The inviscid flow over flared bodies at angle of attack is investigated. Experimental pressure distributions are presented for bodies with a hemispherical nose and with a conical nose. Data are shown for Mach numbers of 5.2, 7.4, and 10.5 and for angles of attack of 0°, 5°, and 10°. The models are provided with a means for removing the boundary layer upstream of the flare to eliminate shock-induced separation.

A perturbation method is developed for the numerical calculation of the flare shock conditions, and the resulting equations are incorporated into a computer program based on the linearized characteristics method. Comparisons are made with experiment and with other more approximate theories which have been developed for flared bodies.

INTRODUCTION

Aircraft and spacecraft designers are often faced with the problem of predicting the aerodynamic forces on bodies that have compression corners on the surface. A particular example is the class of flare-stabilized entry bodies made up of a cylinder followed by a conical frustum. If the flow approaching the flare is locally supersonic, a shock wave is formed near the corner between the cylinder and flare. This shock interacts with the boundary layer on the cylinder ahead of the corner, and the boundary layer perturbs the flow approaching the flare. Thus, calculation of the inviscid and boundary layer flow is coupled, making the analysis of both more difficult. The embedded shock can cause the boundary layer to separate, and can therefore have a large effect on the inviscid flow. The aerodynamic stability at small angles of attack is especially sensitive to this interaction. Even the development of uncoupled inviscid theories has been hindered by the fact that experimental results have usually had various degrees of boundary-layer shock-wave interaction.

Numerous attempts have been made to predict the inviscid flow over flared bodies at incidence (see, e.g., refs. 1 to 5). These existing theories have tended to be empirical and have consisted of patching together various simple flows. While adequate for most preliminary design purposes, these theories have some deficiencies which appear in comparisons with experiment (see ref. 2), and it is not possible to determine whether the differences are due to approximations in the theory or to viscous effects in the experiments. The present paper therefore has a dual purpose. First, an attempt is made to apply exact

numerical methods to determine the perturbations to the flow over flared bodies at incidence. Second, results of experiments are presented in which the effects of boundary-layer interaction have been purposely suppressed by leaving a small gap between the body and the flare through which the boundary layer can escape. The resulting pressure distributions can then be compared directly with inviscid theories and thereby illustrate any deficiencies of the theories.

Computer programs applicable to flared bodies at zero incidence have been developed at Ames Research Center (ref. 6) and elsewhere. A program based on the linearized characteristics method has also been used in references 7 and 8 to calculate the first-order effects of angle of attack for smooth bodies. In the present report the linearized characteristics method is extended and applied to flows with embedded or secondary shocks. The results of sample calculations are compared with experimental pressure distributions obtained from the Ames 3.5-Foot Hypersonic Wind Tunnel. Also, force coefficients and centers of pressure predicted by theory are compared with integrated experimental pressures and with other theories.

SYMBOLS

a	speed of sound
A	reference area, $\frac{\pi d^2}{4}$
C_A	axial force coefficient (excluding viscous and base drag), $\frac{\text{axial force}}{q_\infty A}$
C_N	normal-force coefficient, $\frac{\text{normal force}}{q_\infty A}$
C_p	pressure coefficient, $\frac{p - p_\infty}{q_\infty}$
d	diameter of cylindrical body segment
h	enthalpy
K_B	body curvature
K_W	shock-wave curvature
K_P	pressure gradient along a straight shock
K_θ	flow-angle gradient along a straight shock
M	Mach number, $\frac{V}{a}$
p	pressure
q	dynamic pressure, $\frac{\rho V^2}{2}$

R	radial distance to shock wave
R_b	blunt body nose radius
S	entropy
s,n,t	streamline coordinates (see fig. 1)
u	velocity component in x direction
v	velocity component in r direction
V	scalar magnitude of velocity vector
$\vec{V}$	velocity vector
w	velocity component in circumferential direction (crossflow velocity)
W	distance along a shock wave
x_{cp}	distance to center of pressure
x,r,Φ	cylindrical coordinates
x,y,z	rectangular coordinates
X	distance from center of spherical nose, $X = x - R_b$
α	angle of attack
β	$\sqrt{M^2 - 1}$
γ	specific heat ratio
ϵ	0 for two-dimensional flow, 1 for axisymmetric flow
ζ	angle between shock wave and flow direction
θ	flow angle measured from x axis in meridional plane (see fig. 1), $\tan^{-1}\frac{v}{u}$
ξ,η	characteristic coordinates
ρ	density
σ	shock-wave angle measured from x axis
φ	crossflow angle (see fig. 1), $\sin^{-1} w/V$
Φ	azimuthal coordinate, cylindrical coordinates

Subscripts

B	body boundary condition
d	downstream shock conditions
S	shock boundary condition
u	upstream shock conditions
o	zero-order variable from solution of zero incidence flow field
1	first-order perturbation variable, implies a derivative with respect to α which is a function of x and r only
∞	free-stream conditions
α	derivative with respect to α

Superscripts

A,B, . . .	points in the flow field
'	coordinates fixed with respect to body axes
''	coordinates fixed with respect to shock axes

THEORY

Linearized characteristics theory has been applied to a number of problems involving smooth body shapes (see, e.g., refs. 7 to 9). In this section the method will be applied to bodies with a compression corner which develops a shock embedded in a nonuniform flow field. The corner angle is restricted only by the condition that the shock must be attached and the flow behind the shock supersonic. The equations and boundary conditions are linearized with respect to the angle of attack, α. Thus the method yields information about the first-order changes of the flow field as a result of a small change in angle of attack. It depends on the prior solution of the flow at zero incidence and on prescribed initial conditions. In the present case the solutions for zero incidence are obtained with the computer programs described in references 6 and 10. Initial conditions for pointed bodies are obtained from cone theory as described in reference 8. Initial conditions for spherically blunted bodies, to which present applications are restricted, depend only on the axisymmetric solution which is calculated by the inverse method (ref. 10).

The linearized characteristics equations will be outlined briefly in the following pages, and the boundary conditions for an embedded shock will be derived. The reader who does not care to follow the details of the derivation

may turn directly to the section on Calculation Procedure. One should, however, take note of equations (1) below which define the notation used for the perturbation variables. A sketch of the coordinate axes and flow direction angles is presented in figure 1.

Perturbation Equations

The problem of calculating the perturbation flow field for a body with a compression corner differs from that for a smooth body only in the details of the embedded shock calculation. Therefore, before the embedded shock is discussed the equations used in references 7 and 8 for smooth bodies will be listed. In the present form these equations apply to perfect or real gases in thermodynamic equilibrium. The subscript 0 is used to identify a quantity obtained from the zero angle-of-attack solution (a known quantity), and the subscript 1 is used for the unknown perturbation variables defined by

$$\left.\begin{aligned} p_1(x,r) &= \frac{1}{\cos\Phi}\, p_\alpha(x,r,\Phi) = \frac{1}{\cos\Phi}\left(\frac{\partial p}{\partial \alpha}\right)_{\alpha=0} \\ \theta_1(x,r) &= \frac{1}{\cos\Phi}\, \theta_\alpha(x,r,\Phi) = \frac{1}{\cos\Phi}\left(\frac{\partial \theta}{\partial \alpha}\right)_{\alpha=0} \\ \varphi_1(x,r) &= \frac{1}{\sin\Phi}\, \varphi_\alpha(x,r,\Phi) = \frac{1}{\sin\Phi}\left(\frac{\partial \varphi}{\partial \alpha}\right)_{\alpha=0} \end{aligned}\right\} \tag{1}$$

and so on. One should note that the perturbation variables are independent of the meridional angle, Φ. Therefore the analysis can be made in any meridional plane; the leeward plane of symmetry is chosen in the present case.

The basic perturbation equations, in terms of characteristic coordinates ξ, η, are

$$\frac{\beta_0}{\rho_0 V_0^2}\frac{\partial p_1}{\partial \eta} + \frac{\partial \theta_1}{\partial \eta} = F - G \tag{2a}$$

$$\frac{\beta_0}{\rho_0 V_0^2}\frac{\partial p_1}{\partial \xi} - \frac{\partial \theta_1}{\partial \xi} = E - G \tag{2b}$$

where

$$G = \frac{\varphi_1 + \theta_1 \cos\theta_0}{M_0 r}$$

$$F = \frac{\beta_o}{M_o \rho_o V_o^2}\left[(A + \theta_1)\frac{\partial p_o}{\partial s_o} - (B + \beta_o\theta_1)\frac{\partial p_o}{\partial n_o}\right] + \frac{\theta_1}{M_o}\left(\frac{\partial \theta_o}{\partial s_o} - \beta_o \frac{\partial \theta_o}{\partial n_o}\right)$$

$$E = \frac{\beta_o}{M_o \rho_o V_o^2}\left[(A - \theta_1)\frac{\partial p_o}{\partial s_o} + (B + \beta_o\theta_1)\frac{\partial p_o}{\partial n_o}\right] + \frac{\theta_1}{M_o}\left(\frac{\partial \theta_o}{\partial s_o} + \beta_o \frac{\partial \theta_o}{\partial n_o}\right)$$

and

$$A = \frac{2}{\beta_o V_o^2}\left\{p_1\left[\left(\frac{\partial h}{\partial p}\right)_\rho + V_o M_o^3\left(\frac{\partial a}{\partial p}\right)_\rho\right] + \rho_1\left[\left(\frac{\partial h}{\partial \rho}\right)_p + V_o M_o^3\left(\frac{\partial a}{\partial \rho}\right)_p + \frac{\beta_o^2 V_o^2}{2\rho_o}\right]\right\}$$

$$B = \frac{2}{V_o^2}\left\{p_1\left(\frac{\partial h}{\partial p}\right)_\rho + \rho_1\left[\left(\frac{\partial h}{\partial \rho}\right)_p - \frac{V_o^2}{2\rho_o}\right]\right\}$$

Two additional equations give the gradients of the crossflow angle and entropy perturbations along the zero angle-of-attack streamline, s_o, which is the third characteristic direction. These are

$$\frac{\partial \varphi_1}{\partial s_o} = \left(\frac{1}{\rho_o V_o^2}\frac{\partial p_o}{\partial s_o} - \frac{\sin \theta_o}{r}\right)\varphi_1 + \frac{p_1}{r\rho_o V_o^2} \tag{3}$$

and

$$\frac{\partial S_1}{\partial s_o} = -\theta_1 \frac{dS_o}{dn_o} \tag{4}$$

The energy equation and the equation of state are needed to complete the system of equations. In terms of the perturbation variables these equations take the following form:

Energy

$$h_1 + V_o V_1 = 0 \tag{5}$$

State

$$\left.\begin{aligned} h_1 &= \left(\frac{\partial h}{\partial p}\right)_\rho p_1 + \left(\frac{\partial h}{\partial \rho}\right)_p \rho_1 \\ a_1 &= \left(\frac{\partial a}{\partial p}\right)_\rho p_1 + \left(\frac{\partial a}{\partial \rho}\right)_p \rho_1 \\ S_1 &= \left(\frac{\partial S}{\partial p}\right)_\rho p_1 + \left(\frac{\partial S}{\partial \rho}\right)_p \rho_1 \end{aligned}\right\} \tag{6}$$

The partial derivatives in equations (6) can be written explicitly for a perfect gas but must be found numerically for a real gas as described in reference 8. One supplementary equation that is needed for the present development is

$$w_1 = V_o \varphi_1 \tag{7}$$

which gives the familiar crossflow velocity perturbation in terms of the crossflow angle perturbation that appears in the previous equations.

The initial conditions must specify the perturbation variables along a noncharacteristic line between the body and the shock in a supersonic flow region. At the present time, initial conditions are available only for pointed cones and spheres. In the present paper, application is made only to a spherically tipped body, and the perturbation variables are all zero on the starting line in this case.

Boundary Conditions for Smooth Bodies

Although the equations given above are independent of the particular choice of reference axes, their boundary conditions are not. These conditions will vary depending on the choice of axes. In the present development the boundary conditions are given in terms of wind axes. Thus at the body one has

$$(\theta_1)_B = -1 + (x - R_b)\frac{\partial \theta_o}{\partial r} - r\frac{\partial \theta_o}{\partial x} \tag{8}$$

$$(S_1)_B = K + [(x - R_b)\cos\theta_o + r\sin\theta_o]\frac{dS_o}{dn} \tag{9}$$

where

$$K = \begin{cases} 0 & \text{for a spherical nose} \\ (S_1)_{cone} & \text{for a pointed nose} \end{cases}$$

At the bow shock the perturbation conditions are

$$(p_1)_s = \sigma_1 \frac{dp}{d\sigma} - R_1 \frac{\partial p_o}{\partial r} \tag{10a}$$

$$(\rho_1)_s = \sigma_1 \frac{d\rho}{d\sigma} - R_1 \frac{\partial \rho_o}{\partial r} \tag{10b}$$

$$(\theta_1)_s = \sigma_1 \frac{d\theta}{d\sigma} - R_1 \frac{\partial \theta_o}{\partial r} \tag{10c}$$

$$(\varphi_1)_s = \sigma_1 \left(\frac{V_\infty}{V_o} - \cos \theta_o + \cot \sigma_o \sin \theta_o \right) \tag{11}$$

The two new perturbation parameters introduced in equations (10) and (11) are the shock angular perturbation, σ_1, and radial perturbation, R_1. They are related geometrically by the relation

$$\frac{dR_1}{dx} = \sigma_1 \sec^2 \sigma_o \tag{12}$$

The derivatives with respect to shock angle, σ, can be obtained from the usual shock equations, and are evaluated in appendix A.

Equations (1) through (12) completely specify the perturbation problem for smooth bodies. They apply also for cornered bodies except for the immediate vicinity of the embedded shock. At a corner with an attached shock the term K in equation (9) will change, and all along the shock the jump conditions given in equations (10) and (11) will be complicated by the nonuniform upstream conditions. These generalized shock conditions are developed next.

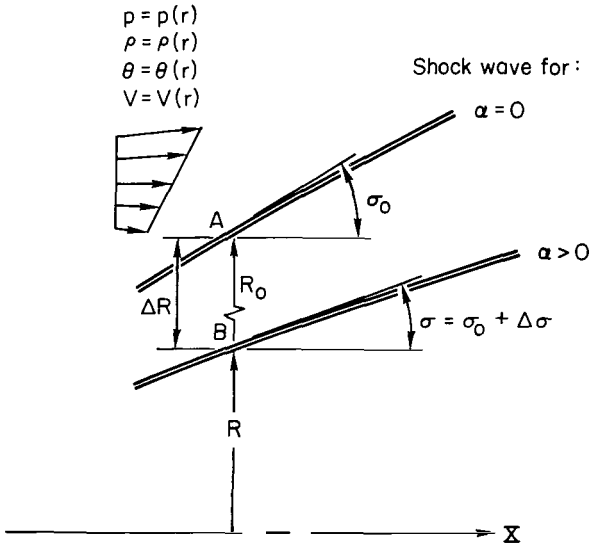

Sketch (a)

Boundary Conditions for an Embedded Shock

Shock conditions for p_1, ρ_1, θ_1.- Consider first a point on the shock some distance from the body and in the leeward plane of symmetry. The upstream conditions are nonuniform and the shock is displaced, as shown in sketch (a), as a result of pitching the body to angle of attack α. For the development of the perturbation shock conditions, it is convenient to introduce a derivative following the shock wave, that is, the rate of change of a quantity with respect to coordinates fixed with the shock wave. Thus the notation $D/D\alpha$ is used to indicate the derivative

$$\frac{Dp}{D\alpha} = \lim_{\alpha \to 0} \left(\frac{p^B - p_o{}^A}{\alpha} \right) \tag{13}$$

In terms of the original notation defined in equations (1), one may write, making use of a double prime superscript

$$\left.\begin{aligned} p_1''(x,r) &\equiv \frac{1}{\cos \Phi} \frac{Dp(x,r,\Phi)}{D\alpha} \\ \theta_1''(x,r) &\equiv \frac{1}{\cos \Phi} \frac{D\theta(x,r,\Phi)}{D\alpha} \\ \varphi_1''(x,r) &\equiv \frac{1}{\sin \Phi} \frac{D\varphi(x,r,\Phi)}{D\alpha} \end{aligned}\right\} \tag{14}$$

The derivative $D/D\alpha$ can be written in a more suitable form by expanding flow variables in a series in terms of the radial distance from point A. Using the pressure as an example, one has

$$p^B = p^A + \Delta R \left(\frac{\partial p}{\partial r} \right)^A + O(\Delta R^2) \tag{15}$$

The perturbation expansions, in terms of wind axes,

$$\left.\begin{aligned} p^A &= p_o{}^A + \alpha p_1{}^A + O(\alpha^2) \\ \Delta R &= \alpha R_1{}^A + O(\alpha^2) \end{aligned}\right\} \tag{16}$$

are now introduced in equation (15), and the result substituted into equation (13). (Note that the subscripts 1 and α are synonymous here since the analysis is made in the plane $\Phi = 0$.) Terms of order α^2 are eliminated in the limiting process, and there results

$$\frac{Dp}{D\alpha} = p_1 + R_1 \left(\frac{\partial p_o}{\partial r} \right) \tag{17}$$

where it is understood that all quantities are evaluated at point A. This gives the first-order expansion of the shock derivative in terms of quantities evaluated in wind axes. Since the present calculations are made in terms of wind axes, the necessary shock conditions can now be easily formulated with the use of equation (17). The equations giving the jump conditions across a shock wave may be written generally as

$$\left.\begin{aligned} p_d &= p(p_u, \rho_u, V_u, \zeta_u) \\ \rho_d &= \rho(p_u, \rho_u, V_u, \zeta_u) \\ \theta_d - \theta_u &= \theta(p_u, \rho_u, V_u, \zeta_u) \end{aligned}\right\} \tag{18}$$

where

$$\zeta_u = \sigma - \theta_u \tag{19}$$

and the subscripts d and u refer to conditions downstream and upstream from the shock wave, respectively. Differentiating equations (18) yields

$$\left.\begin{aligned}
\frac{Dp_d}{D\alpha} &= \frac{\partial p}{\partial p_u}\frac{Dp_u}{D\alpha} + \frac{\partial p}{\partial \rho_u}\frac{D\rho_u}{D\alpha} + \frac{\partial p}{\partial V_u}\frac{DV_u}{D\alpha} + \frac{\partial p}{\partial \zeta_u}\frac{D\zeta_u}{D\alpha} \\
\frac{D\rho_d}{D\alpha} &= \frac{\partial \rho}{\partial p_u}\frac{Dp_u}{D\alpha} + \frac{\partial \rho}{\partial \rho_u}\frac{D\rho_u}{D\alpha} + \frac{\partial \rho}{\partial V_u}\frac{DV_u}{D\alpha} + \frac{\partial \rho}{\partial \zeta_u}\frac{D\zeta_u}{D\alpha} \\
\frac{D\theta_d}{D\alpha} - \frac{D\theta_u}{D\alpha} &= \frac{\partial \theta}{\partial p_u}\frac{Dp_u}{D\alpha} + \frac{\partial \theta}{\partial \rho_u}\frac{D\rho_u}{D\alpha} + \frac{\partial \theta}{\partial V_u}\frac{DV_u}{D\alpha} + \frac{\partial \theta}{\partial \zeta_u}\frac{D\zeta_u}{D\alpha}
\end{aligned}\right\} \tag{20}$$

These equations contain a 4×3 matrix of partial derivatives with respect to upstream conditions. Evaluation of these derivatives from equations (18) is discussed in detail in appendix A. The presence in equations (20) of these upstream derivatives is one essential difference between the embedded shock conditions and equations (10) for the bow shock with uniform upstream conditions. In the case of uniform upstream conditions, only derivatives with respect to ζ_u remain in equations (20), and these may be written, without loss of generality, as

$$\frac{\partial}{\partial \zeta_u} = \frac{\partial}{\partial \sigma} \tag{21}$$

since the partial derivative implies that θ_u is constant. However, all of the terms in equations (20) must be retained for the present problem.

The last step needed to put the shock conditions into their desired form is to introduce equation (17) into equations (20). The result (noting that $\partial\sigma_o/\partial r = 0$) is

$$p_{1d} = \sigma_1 \frac{\partial p}{\partial \sigma} - R_1\left(\frac{\partial p_{od}}{\partial r} - \frac{\partial p}{\partial p_u}\frac{\partial p_{ou}}{\partial r} - \frac{\partial p}{\partial \rho_u}\frac{\partial \rho_{ou}}{\partial r} - \frac{\partial p}{\partial V_u}\frac{\partial V_{ou}}{\partial r} + \frac{\partial p}{\partial \sigma}\frac{\partial \theta_{ou}}{\partial r}\right)$$

$$+ \left(p_{1u}\frac{\partial p}{\partial p_u} + \rho_{1u}\frac{\partial p}{\partial \rho_u} + V_{1u}\frac{\partial p}{\partial V_u} - \theta_{1u}\frac{\partial p}{\partial \sigma}\right) \tag{22a}$$

$$\rho_{1d} = \sigma_1 \frac{\partial \rho}{\partial \sigma} - R_1\left(\frac{\partial \rho_{od}}{\partial r} - \frac{\partial \rho}{\partial p_u}\frac{\partial p_{ou}}{\partial r} - \frac{\partial \rho}{\partial \rho_u}\frac{\partial \rho_{ou}}{\partial r} - \frac{\partial \rho}{\partial V_u}\frac{\partial V_{ou}}{\partial r} + \frac{\partial \rho}{\partial \sigma}\frac{\partial \theta_{ou}}{\partial r}\right)$$

$$+\left(p_{1u}\frac{\partial \rho}{\partial p_u} + \rho_{1u}\frac{\partial \rho}{\partial \rho_u} + V_{1u}\frac{\partial \rho}{\partial V_u} - \theta_{1u}\frac{\partial \rho}{\partial \sigma}\right) \tag{22b}$$

$$\theta_{1d} = \sigma_1 \frac{\partial \theta}{\partial \sigma} - R_1\left[\frac{\partial \theta_{od}}{\partial r} - \frac{\partial \theta}{\partial p_u}\frac{\partial p_{ou}}{\partial r} - \frac{\partial \theta}{\partial \rho_u}\frac{\partial \rho_{ou}}{\partial r} - \frac{\partial \theta}{\partial V_u}\frac{\partial V_{ou}}{\partial r} + \left(\frac{\partial \theta}{\partial \sigma} - 1\right)\frac{\partial \theta_{ou}}{\partial r}\right]$$

$$+\left[p_{1u}\frac{\partial \theta}{\partial p_u} + \rho_{1u}\frac{\partial \theta}{\partial \rho_u} + V_{1u}\frac{\partial \theta}{\partial V_u} - \theta_{1u}\left(\frac{\partial \theta}{\partial \sigma} - 1\right)\right] \tag{22c}$$

Equations (22) are the desired generalizations of equations (10). They contain additional terms which reflect the presence of upstream gradients in the basic zero incidence flow field, and upstream perturbations due to incidence. These upstream influences are multiplied by weighting factors determined from the shock equations. The weighting factors are the partial derivatives evaluated in appendix A.

Shock conditions for the crossflow angle, φ_1.- The condition on the crossflow angle is somewhat simpler due to the fact that $\varphi = 0$ everywhere for zero incidence. The present derivation is therefore basically the same as that given in greater detail in reference 7. An additional term will appear, however, which is due to the crossflow angle perturbation upstream of the shock.

In terms of shock oriented coordinates, it is clear that

$$w''_{1d} = w''_{1u} \tag{23}$$

This equation states that the velocity component tangent to the shock is unchanged as required by the momentum equation. Use of equation (7) then gives

$$\varphi''_{1d} = \frac{V_{ou}}{V_{od}}\varphi''_{1u} \tag{24}$$

The following equation, derived in reference 7 to transform φ from shock to wind axes,

$$\varphi_1 = \varphi_1'' - \sigma_1(\cos\theta_o - \cot\sigma_o \sin\theta_o) \tag{25}$$

may be applied to equation (24) with the result

$$\varphi_{1d} + \sigma_1(\cos\theta_{od} - \cot\sigma_o \sin\theta_{od}) = \frac{V_{ou}}{V_{od}}\left[\varphi_{1u} + \sigma_1(\cos\theta_{ou} - \cot\sigma_o \sin\theta_{ou})\right]$$

or

$$\varphi_{1d} = \left(\frac{V_{ou}}{V_{od}}\right)\varphi_{1u} - \sigma_1\left[\left(\cos\theta_{od} - \frac{V_{ou}}{V_{od}}\cos\theta_{ou}\right) - \cot\sigma_o\left(\sin\theta_{od} - \frac{V_{ou}}{V_{od}}\sin\theta_{ou}\right)\right] \tag{26}$$

For the bow shock wave

$$\varphi_{1u} = 0$$

and

$$\theta_{ou} = 0$$

so that equation (26) reduces to equation (11). However, for a shock embedded in a nonuniform field, the more general expression (26) is needed.

Shock conditions at the corner.- The shock conditions derived above depend linearly on the shock angular perturbation, σ_1, and the radial perturbation, R_1. The calculation of these shock perturbation parameters for a general shock point will be outlined in the next section. Their initial values, at the surface of the body, are calculated in a different manner as outlined in the present section.

Just as the shock conditions are most easily found with the use of shock oriented coordinates, the present analysis is simplified by body axes. Variables expressed in body axes will be identified by a prime superscript. Referring to sketch (b), one has

A. Position of corner for $\alpha = 0$
B. Position of corner for $\alpha > 0$

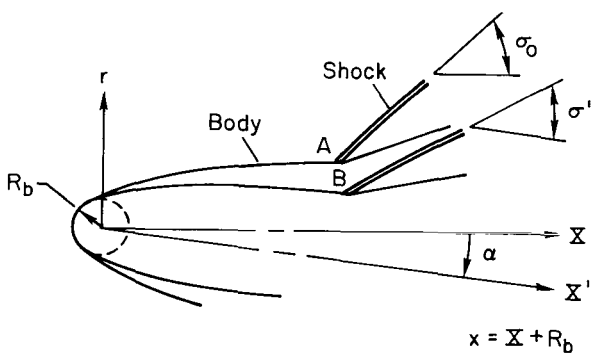

Sketch (b)

$$p_1' \cos\Phi' = \lim_{\alpha\to 0}\left(\frac{p^B - p_o{}^A}{\alpha}\right) \tag{27}$$

In terms of body axes, the surface boundary condition is

$$(\theta_1')_B = 0 \tag{28}$$

for both the upstream and downstream flow-angle perturbations. Making use of this condition, while differentiating the shock relations (eqs. (18)), one obtains

$$p'_{1d} = \sigma_1' \frac{\partial p}{\partial \sigma} + p'_{1u} \frac{\partial p}{\partial p_u} + \rho'_{1u} \frac{\partial p}{\partial \rho_u} + V'_{1u} \frac{\partial p}{\partial V_u} \tag{29a}$$

$$\rho'_{1d} = \sigma_1' \frac{\partial \rho}{\partial \sigma} + p'_{1u} \frac{\partial \rho}{\partial p_u} + \rho'_{1u} \frac{\partial \rho}{\partial \rho_u} + V'_{1u} \frac{\partial \rho}{\partial V_u} \tag{29b}$$

$$\theta'_{1d} = 0 = \sigma_1' \frac{\partial \theta}{\partial \sigma} + p'_{1u} \frac{\partial \theta}{\partial p_u} + \rho'_{1u} \frac{\partial \theta}{\partial \rho_u} + V'_{1u} \frac{\partial \theta}{\partial V_u} \tag{29c}$$

The partial derivatives used here are those introduced in equations (20). Equation (29c) gives the initial value of the shock angular perturbation in terms of body axes

$$\sigma_1' = \frac{-1}{\partial\theta/\partial\sigma} \left(p'_{1u} \frac{\partial \theta}{\partial p_u} + \rho'_{1u} \frac{\partial \theta}{\partial \rho_u} + V'_{1u} \frac{\partial \theta}{\partial V_u} \right) \tag{30}$$

The shock radial perturbation is, of course, zero when following the body

$$(R_1')_B = 0 \tag{31}$$

Equations (29a) and (29b) together with the equation of state (eqs. (6)) yield the jump condition for the entropy perturbation[1]

$$S'_{1d} = \left(\frac{\partial S}{\partial p} \right)_\rho p'_{1d} + \left(\frac{\partial S}{\partial \rho} \right)_p \rho'_{1d} \tag{32}$$

which, in turn, defines the new value for the constant, K, in equation (9); that is

$$K = S'_{1d} \tag{33}$$

downstream of the corner.

Equations (29) to (33) complete the boundary conditions for the corner, but they must be converted to wind axes to be consistent with the rest of the analysis. This conversion has been discussed in detail in reference 7, and only the results will be given here. These are:

[1]The condition, K = 0 in equation (9), implies a constant entropy on the surface of a spherically tipped body at incidence. It is noteworthy that behind a corner the entropy varies as cos Φ' in accordance with equation (32). This is an example of a situation where a body at incidence does not have a constant entropy everywhere on its surface.

$$\left.\begin{aligned} p_1 &= p_1' + (x - R_b)\frac{\partial p_o}{\partial r} - r\frac{\partial p_o}{\partial x} \\ \rho_1 &= \rho_1' + (x - R_b)\frac{\partial \rho_o}{\partial r} - r\frac{\partial \rho_o}{\partial x} \\ V_1 &= V_1' + (x - R_b)\frac{\partial V_o}{\partial r} - r\frac{\partial V_o}{\partial x} \end{aligned}\right\} \tag{34}$$

$$R_1 = R_1' - R_o \tan \sigma_o - (x - R_b) \tag{35}$$

$$\sigma_1 = \sigma_1' - 1 - R_o \frac{d\sigma_o}{dx} \tag{36}$$

The transformations for entropy and flow angle have already been given in equations (8) and (9) above, and equation (26) for the crossflow angle applies here also without change. The derivative, $d\sigma_o/dx$, appearing in equation (36) is related to the shock curvature at zero incidence. It will not, in general, be zero when the upstream conditions are nonuniform. The derivative of the shock angle with respect to x can be obtained from the shock curvature which is evaluated in appendix A.

This completes the specification of the perturbation shock conditions in a nonuniform stream. The next section presents a brief description of how the calculation of a typical shock point is performed.

Calculation Procedure

The equations and boundary conditions presented in the previous sections can be used to calculate numerically the entire perturbation field on a characteristic mesh evaluated for zero incidence. This calculation has been programmed in conjunction with the axisymmetric program described in reference 6. After each point in the field is solved for $\alpha = 0$, the gradients of the axisymmetric field are evaluated, and the perturbation equations solved. The calculation for smooth bodies is described in reference 7. In this section the details of the embedded shock calculation are outlined.

Gradients of the $\alpha = 0$ field.- The coefficients of the perturbation equations and the boundary conditions contain derivatives, or gradients, of the zero incidence flow variables, p_o, ρ_o, θ_o, V_o, S_o. These gradients play an important part in the solution, and in the shock conditions in particular. For a general field point, a simple, linear backward difference method is sufficiently accurate to give good results. However, immediately behind a shock wave, such methods are not satisfactory, in general. A method which makes use of the shock curvature in conjunction with the equations of motion was therefore adopted and is described in appendix A.

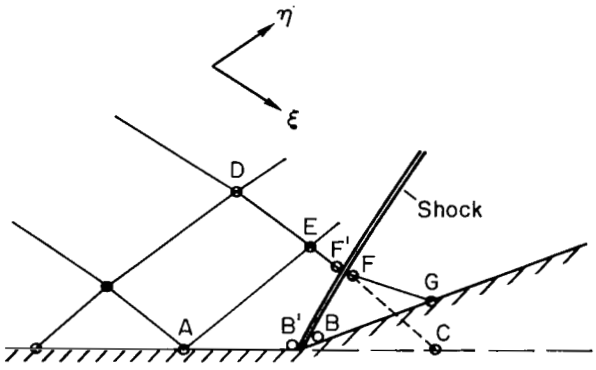

Sketch (c)

Corner point.- A typical characteristic mesh in the vicinity of a corner is shown in sketch (c). The fictitious point C (later to be discarded) is first calculated in the usual way by neglecting the corner. Conditions upstream of the shock at point B' are then calculated by linear interpolation between A-C, and at point F' by interpolation along D-E-C. Conditions at point B, downstream of the shock, are then obtained by straightforward application of equations (29) to (36). The calculation of conditions at point F is different from that for a general shock point since the field downstream of the shock is unknown at this stage in the calculation. An approximation to the shock angular perturbation, σ_1, at point F is obtained if the corner boundary condition (eq. (28)) is assumed to apply there. This assumes that $d\sigma_1/dx$ is small. Downstream conditions at point F can then be obtained with equations (29) to (36), and with corresponding upstream conditions.

In the first attempts to perform the numerical calculations, the shock angle at point F was assumed equal to the value on the body at point B. This procedure, which neglects $d\sigma_0/dx$, was used successfully in reference 6 for zero incidence flows, but it caused large errors in the present perturbation solution. It was thus necessary to calculate the shock curvature at point B, and make use of this information to obtain a better approximation to the shock angle, σ_0, at point F. The equations developed in appendix A were used for this purpose.

General shock point.- A typical characteristic mesh for a general shock point is shown in sketch (d). The fictitious point D is first calculated, and upstream conditions at point C' are obtained by linear interpolation along DE. Conditions at point A are also obtained by interpolation using points B and F (these are known from the previous shock point or, initially, from the corner point). One can now apply equation (2a) along the η coordinate from A to C, equation (12) along the shock from B to C, and equations (22a) and (22c) at point C. These are written in finite difference form as follows:

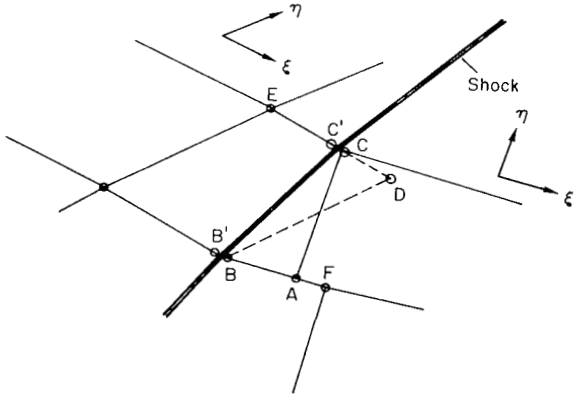

Sketch (d)

$$a(p_1^C - p_1^A) + (\theta_1^C - \theta_1^A) = (F - G)\Delta\eta \qquad (37)$$

$$R_1^C = R_1^B + b(\sigma_1^B + \sigma_1^C) \tag{38}$$

$$p_1^C = \sigma_1^C \frac{\partial p}{\partial \sigma} - R_1^C d + e \tag{39}$$

$$\theta_1^C = \sigma_1^C \frac{\partial \theta}{\partial \sigma} - R_1^C f + g \tag{40}$$

where

$$a = \frac{\beta_o}{\rho_o V_o^2}$$

$$b = \frac{1}{2}(x^C - x^B)\sec^2 \sigma_o$$

and d, e, f, and g can be identified by comparing equations (39) and (40) with equations (22a) and (22c). The four equations (37) to (40) in terms of the unknowns p_1^C, θ_1^C, σ_1^C, and R_1^C can be solved for σ_1^C. All of the remaining variables are then obtained by direct substitution. The procedure is iterated, making use of average values for the coefficients, until convergence of the pressure perturbation, p_1^C, is obtained.

The inviscid theory developed in the preceding pages is an exact numerical solution to the first-order angle-of-attack perturbation of the flow field; that is, it yields the exact initial slope of the pressure and other flow variables. The largest angle of attack for which this linear approximation may be applied depends, of course, on the degree of nonlinearity of the actual flow. This nonlinearity can be assessed at present only by comparison with the proper experiment. An experimental program suited to this purpose has been conducted and will be described in the following section.

EXPERIMENT

In order to check the applicability of the perturbation theory, and to provide basic pressure data, a test program was conducted with the models shown in figure 2. A brief description of these tests follows.

Facilty and Test Procedure

The experimental study was conducted in the Ames 3.5-Foot Hypersonic Blowdown Wind Tunnel at Mach numbers of 5.2, 7.4, and 10.5 and stagnation pressures of 13.6, 102.0, and 122.5 atmospheres (200, 1500, and 1800 psi), respectively, and at a constant stagnation temperature of 1166° K. The corresponding Reynolds numbers based on model length were approximately 0.9×10^6 at M = 5.2, 3.5×10^6 at M = 7.4, and 1.7×10^6 at M = 10.5. Data were taken at angles of attack of approximately 0°, 5°, and 10° during an average total testing time of approximately 1 minute. A more general description of the test facility and its instrumentation is given in reference 11. A recent modification to the facility permits the test models to be inserted into the test section only

during the period when steady flow exists. This innovation was used for the present tests and greatly alleviates the effects of heating and stopping loads on the test models and instrumentation.

Models and Apparatus

The models were constructed of stainless steel and consisted of two interchangeable noses, a cylindrical center section, and conical flare with a flare angle of 16.5°. The nose shapes were a hemisphere and a $22\text{-}1/2^{\circ}$ half-angle cone. A photograph of the hemispherical-nose model is shown in figure 2(a) while a dimensional sketch, along with other details of the test models, is presented in figure 2(b). The technique used in constructing the flare proved to be successful in bleeding off the boundary layer and, hence, in eliminating flare-induced separation on the cylindrical portion of the body (see ref. 12). It consisted of making the flare hollow and providing a gap between the flare and body cylinder. A gap size of 5 percent of the diameter of the body cylinder was found to be suitable for the present tests. This gap size was slightly in excess of the maximum boundary-layer thickness at the flare estimated for the present models and test conditions. Preliminary tests were also made in which the gap size was varied from about 3 to 6 percent to determine if the pressures in the vicinity of the flare were affected. The results of these tests showed that the magnitude of the body pressures was not affected as long as the size of the flare gap was sufficiently large to prevent separation. Visible surface films were used in these tests to verify that boundary-layer separation had been eliminated with the chosen gap.

The models were provided with thirty-nine 1.07 mm (0.042 in.) diameter pressure orifices distributed in two rows, 180° apart. Stainless-steel pressure tubing, 1.59 mm O.D. (0.0625 in.), was brazed into the walls of the models and led out through the base of the flare. About 3 feet aft of the flare, the stainless-steel tubing was joined to Viton high-temperature, flexible tubing, 0.79 mm I.D. (0.0375 in.) and 3.18 mm O.D. (0.125 in.), which led to the pressure cells. The total length of pressure tubing was about 4 meters. A table giving the location of the pressure orifices on the test models is presented in figure 2(b).

Instrumentation and Accuracy of Results

The three ranges of strain-gage pressure cells employed in the tests were 0.34, 0.68, and 3.4 atmospheres (5, 10, and 50 psi). The cells were chosen to give maximum accuracy in measuring the pressures at a given model location for each test condition. Also, the pressure which was anticipated to be lowest was monitored on an oscillograph, and the data were recorded when this pressure stabilized. The precision of the final experimental data in coefficient form depends upon the accuracy in measuring the free-stream and orifice pressures and on the uncertainty in determining the free-stream dynamic pressure. The estimated over-all error in the pressure coefficient due to these uncertainties is ± 0.007. The maximum estimated error in angle of attack, including possible variations in free-stream angularity, was $\pm 0.3^{\circ}$.

RESULTS AND DISCUSSION

Surface Pressures and Shock Shapes

The experimental results for body surface pressures in coefficient form are presented in figures 3 and 4 for the hemispherical- and conical-nose models, respectively. Results for the hemispherical-nose model are given for Mach numbers of 5.2, 7.4, and 10.5 and at angles of attack of 0°, 5°, and 10°, while the results for the conical-nose model are given for Mach numbers of 5.2 and 7.4 and angles of attack of 0° and 5°.

Numerical calculations for the surface pressures on the spherical-nose model are also shown in figure 3. Theory and experiment are in agreement for $\alpha = 0^\circ$, but differ, especially on the flare, for other angles of attack. The probable cause of this difference is discussed in the following paragraph. Since perturbation theory has not yet been developed for the expansion corner on the conical-nose model, the numerical results in figure 4 are only for $\alpha = 0^\circ$, and agreement with experiment is excellent. In figure 5 calculated shock shapes are compared with experimental results from shadowgraph pictures for the blunt-nose model at a Mach number of 7.4. As the model is pitched to angles of attack of 5° and 10°, the bow shock remains unchanged relative to V_∞, while the flare shock must move with the body. The flare shock also moves relative to the body, becoming closer to the body on the windward side and farther removed on the leeward side. The calculated shock shapes on the leeward side and for $\alpha = 0^\circ$ agree well with experiment. On the windward side the experimental shock is somewhat steeper and farther from the body than the calculated result.

Circumferential pressure distribution.- The comparison between theoretical and experimental flare pressures for the spherical-nose model at incidence (fig. 3) is not particularly good, even for 5° angle of attack. At 10° angle of attack the experimental pressure is considerably higher than predicted by the theory. On the other hand, the agreement on the spherical nose and on the forward section of the cylinder at $\alpha = 5^\circ$ is very good. The reason for the disagreement between theory and experiment on the rearward portion of the body was studied in some detail and is attributed to the increased importance of second order (α^2) terms neglected in the theory.

In order to illustrate this point, one must look at the second-order term in the expansion of the pressure. The series expansion in α and Φ has the general form (see, e.g., ref. 13)

$$p = p_0 + \alpha p_1 \cos \Phi + \alpha^2(p_2 + p_3 \cos 2\Phi) + O(\alpha^3) \tag{41a}$$

or

$$p = p_0 + \alpha p_1 \cos \Phi + \alpha^2[(p_2 - p_3) + 2p_3 \cos^2 \Phi] + O(\alpha^3) \tag{41b}$$

Thus if the pressure is plotted as a function of $\cos \Phi = z$, the second-order effect would appear as a displacement of the ordinate at $z = 0$ by $\alpha^2(p_2 - p_3)$, and by a curvature $(\partial^2 p/\partial z^2)$ of $4\alpha^2 p_3$. To determine if important second-order

effects were present in the data, additional tests were made with pressure orifices located in various Φ planes. These data are plotted versus $\cos \Phi$ in figure 6 for several x stations ahead of the flare; figure 6(a) is for $\alpha = 5^\circ$ and figure 6(b) for $\alpha = 10^\circ$. Shown also are the linear pressure distributions predicted by the theory. For 5° angle of attack the experimental variation is reasonably linear, although for $x/d = 2.29$ there is a tendency toward a nonlinear variation. For $\alpha = 10^\circ$, the first station ($x/d = 0.45$), which is on the sphere, shows a slightly nonlinear variation, and at rearward stations the experimental pressure distribution is increasingly nonlinear. There is a positive curvature to the pressure distribution at $\cos \Phi = 0$ which can be attributed to the term $\alpha^2 p_3$ in equation (41b). In figure 7 similar data are shown for the flare pressures which also show this second-order effect, becoming very pronounced at $\alpha = 10^\circ$. On the flare these effects are amplified by the pressure rise across the shock.

The discrepancy between theory and experiment is serious when detailed pressure distributions are desired. A need for more exact calculations, or estimates of the second-order term is clearly indicated. However, the linear theory may still be useful for predicting normal forces and moments at angles of attack much larger than that indicated by the comparisons with pressure data. The reason is that when equations (41) are used for the integration of normal forces with respect to Φ, the second-order term is identically zero. Any nonlinearity in C_N and C_m (outside of viscous effects) must therefore be third order in α. These force coefficients and the center of pressure for the blunt-nose model are discussed next.

Force Coefficients and Center of Pressure

Integration of experimental pressures.- In order to evaluate the forces on the model at angle of attack it is, in general, necessary to integrate both in the circumferential and the longitudinal directions. For small angles of attack the circumferential pressure distribution has a cosine variation, and can therefore be integrated exactly. However, for the angles of attack of the present tests, it was found that the pressures deviate from the cosine curve. Nevertheless, by means of arguments given in the previous paragraph and illustrated in figures 6 and 7, it is seen that the deviation is in the same direction, and nearly equal, on the windward and leeward sides. In the case of the normal force and pitching moment, the additions to the cosine variation on windward and leeward sides of the body cancel. Therefore the experimental pressures in the plane of symmetry were used in conjunction with a cosine circumferential distribution to calculate the forces and moments. A cosine distribution was also assumed in calculating the axial force, even though the second-order effects on opposite sides of the body do not cancel in this case. As a result, the experimental data for C_A should be slightly high at angle of attack. The error, however, is believed to be small since it occurs primarily on the flare which accounts for less than 10 percent of the total axial force at the test Mach numbers. Experimental data for the slope of the normal-force coefficient and the center of pressure at $\alpha = 0^\circ$ were calculated with the 5° angle-of-attack data.

Comparison with theory.- Aerodynamic coefficients obtained by integrating the experimental pressure distributions for the spherically blunted model are presented in figures 8 and 9. Figure 8 shows the effect of angle of attack for $M_\infty = 7.4$, and figure 9 shows the variation with Mach number for $\alpha = 0^\circ$. Experimental results for the normal-force coefficient, axial-force coefficient, and center of pressure are compared with the present theory and with the theories of references 2 and 3. The latter methods make use of a combination of simple theories. Jorgensen (ref. 2) assumes a linear pressure variation on the cylinder and applies cone theory to the flare. Seiff (ref. 3) makes use of blast-wave theory on the cylinder and Newtonian theory on the flare. Both of these methods as well as the present numerical results account for the nose contribution by means of modified Newtonian impact theory.

In comparing results for varying angle of attack (fig. 8), one should note that the theories shown give only linear estimates. On the other hand, the experimental results exhibit the actual nonlinear nature of the aerodynamic parameters shown. This effect can be observed in the normal-force, axial-force, and center-of-pressure data which are all slightly high at 10° angle of attack relative to linear extrapolations of the lower angle data. Such trends are expected; however, attention is called to the previous section where reasons were given for expecting the experimental value for C_A to be slightly high.

For 5° angle of attack the experimental data are in best over-all agreement with the present numerical calculations. All the theories give essentially the same axial force, but there are sizable differences in normal force and center of pressure. The method of Jorgensen (ref. 2) predicts normal-force and center-of-pressure values about 10 percent higher than the present method; Seiff's method (ref. 3) overpredicts the normal force by about 30 percent but gives the same center of pressure as the present method. However, the latter agreement is only for a Mach number of 7.4, as can be seen in figure 9.

The comparisons at other Mach numbers between experiment and the various theories are shown in figure 9. Again good agreement is evidenced for the axial-force coefficient, owing mainly to the fact that the nose is the main contributor to this force. The present method gives the best agreement with experimental normal-force slopes, $(C_{N_\alpha})_{\alpha=0}$, and the estimates of reference 3 are consistently high, while those of reference 2 tend to be slightly high at lower Mach numbers. With regard to the center of pressure, $(x_{cp}/d)_{\alpha=0}$, the situation is somewhat reversed. Seiff's method gives the best over-all agreement with the experimental center of pressure, while Jorgensen's method predicts a curve nearly parallel to the data but about 8 percent too high. The present method predicts a greater forward shift of center of pressure with increasing Mach number than that indicated by experiment.

As a consequence of overestimating the normal force, the method of reference 3 also overpredicts the pitching moment. This result was observed in comparisons with data obtained from free-flight tests which were reported in references 4 and 14. The moment-curve slopes obtained from these free-flight tests decrease more rapidly, with increasing Mach number, than the predictions of Seiff's theory (see ref. 14). This trend is in general agreement with the center-of-pressure curve obtained from the present numerical results, but not with the trend of present experimental data, which shows nearly the same center

of pressure at Mach numbers of 7.4 and 10.5. In view of this difference between present numerical calculations and experiment, additional data at higher Mach numbers are needed to verify the predicted shift of the center of pressure.

CONCLUDING REMARKS

The present study was undertaken to provide a better understanding of the inviscid flow over flared bodies at angle of attack. Pressure distributions on flared models, with hemispherical and conical noses, were measured at Mach numbers of 5.2, 7.4, and 10.5. The flares on these models were provided with a means for boundary-layer removal in order to eliminate the large separated-flow region which would have been produced by the flare shock. The experimental pressure distributions therefore correspond to an idealized flow in which large-scale viscous effects have been suppressed. With the nature of the inviscid flow field thus established, the task of understanding flows complicated by viscous effects (which is the usual case) should be simplified.

A linearized perturbation method was developed for the numerical calculation of the flare shock conditions for small angles of attack, and the resulting equations were incorporated into a computer program based on the linearized characteristics method. While this method can be regarded as being exact for sufficiently small angles of attack, comparison with the experimental pressure distributions showed significant deviations on the flare even for 5° angle of attack. Since the experimental results were free of the effects of viscous separation, it was possible to show that the difference between theory and experiment was probably due to second-order (α^2) terms neglected in the present method. These second-order effects cause the circumferential pressure variation to depart from the cosine curve assumed in the perturbation theory. However, the departure from a cosine variation is an even function (i.e., $\cos^2 \Phi$) and therefore does not produce a cross force. (This is in contrast to the second-order effects studied in ref. 15, which are caused by viscosity and which result in a cross force.)

The mutual cancellation of pressures on windward and leeward surfaces thus results in normal forces and pitching moments which are more linear with α than would be anticipated from a knowledge of pressure distributions only in the plane of symmetry. The present theory was therefore useful for estimating the normal-force curve and the center of pressure for angles of attack of about 5°. Comparisons were made with more approximate theories, which are also linearized with respect to angle of attack. The present method was in best over-all agreement with the experimental results, but it predicted a greater decrease in stability with increasing Mach number than was measured experimentally.

Ames Research Center
National Aeronautics and Space Administration
Moffett Field, Calif., Oct. 6, 1965

APPENDIX A

EVALUATION OF SHOCK DERIVATIVES AND FLOW GRADIENTS BEHIND A SHOCK

Calculation of the perturbation flow over a body at incidence requires the knowledge of gradients of the zero incidence field. Evaluation of the field gradients immediately behind a shock wave is accomplished with the use of the equations of motion in conjunction with certain partial derivatives which were introduced in the shock boundary conditions. These partial derivatives describe the downstream influence of unit changes in the shock angle and conditions upstream of the shock. The calculation of the shock derivatives from the oblique shock equations is first described. The equations for flow-field gradients are then derived and their application to the calculation of the shock-wave curvature is illustrated.

SHOCK-WAVE DERIVATIVES

It is convenient to use index notation where f_i are the unknown conditions downstream of the shock wave, and g_k are the known upstream conditions. Then the shock equations which determine the downstream conditions may be written symbolically as (cf. eqs. (18))

$$f_i = f_i(g_1, g_2, g_3, g_4) \tag{A1}$$

In particular, the variables are identified as

$$f_i = p, \rho, \theta \qquad \text{for} \quad i = 1 \rightarrow 3$$

and

$$g_k = p_u, \rho_u, V_u, \zeta_u \qquad \text{for} \quad k = 1 \rightarrow 4$$

where

$$\zeta_u = \sigma - \theta_u$$

Differentiating (A1) with respect to α, as in equations (20), gives

$$\frac{Df_i}{D\alpha} = \sum_{k=1}^{4} \frac{\partial f_i}{\partial g_k} \frac{Dg_k}{D\alpha} \tag{A2}$$

where the tensor $\partial f_i / \partial g_k$ consists of the 4×3 matrix

$$\frac{\partial f_i}{\partial g_k} = \begin{pmatrix} \frac{\partial p}{\partial p_u} & \frac{\partial p}{\partial \rho_u} & \frac{\partial p}{\partial V_u} & \frac{\partial p}{\partial \zeta_u} \\ \frac{\partial \rho}{\partial p_u} & \frac{\partial \rho}{\partial \rho_u} & \frac{\partial \rho}{\partial V_u} & \frac{\partial \rho}{\partial \zeta_u} \\ \frac{\partial \theta}{\partial p_u} & \frac{\partial \theta}{\partial \rho_u} & \frac{\partial \theta}{\partial V_u} & \frac{\partial \theta}{\partial \zeta_u} \end{pmatrix} \tag{A3}$$

which can be evaluated from equation (A1). For a perfect gas, the shock equations given in reference 16 are used to obtain explicit relations for the elements of (A3). These are listed below:

$$\frac{\partial p}{\partial p_u} = -\left(\frac{\gamma - 1}{\gamma + 1}\right) \tag{A4}$$

$$\frac{\partial \rho}{\partial p_u} = -\frac{\dfrac{2\gamma/(\gamma + 1)}{V_u^2 \sin^2 \sigma}}{\left[\left(\dfrac{\gamma - 1}{\gamma + 1}\right) + \left(\dfrac{2\gamma}{\gamma + 1}\right)\dfrac{p_u}{\rho_u V_u^2 \sin^2 \sigma}\right]^2} \tag{A5}$$

$$\frac{\partial \theta}{\partial p_u} = -\sin^2 \theta \tan \sigma \frac{\left(\dfrac{\gamma + 1}{2\gamma}\right)\dfrac{\rho_u V_u^2}{p_u^2}}{\left(\dfrac{\rho_u V_u^2}{\gamma p_u} \sin^2 \sigma - 1\right)^2} \tag{A6}$$

$$\frac{\partial p}{\partial \rho_u} = \frac{2V_u^2 \sin^2 \sigma}{\gamma + 1} \tag{A7}$$

$$\frac{\partial \rho}{\partial \rho_u} = \frac{\left[\left(\dfrac{\gamma - 1}{\gamma + 1}\right) + \left(\dfrac{2\gamma}{\gamma + 1}\right)\dfrac{p_u}{\rho_u V_u^2 \sin^2 \sigma}\right] + \left[\left(\dfrac{2\gamma}{\gamma + 1}\right)\dfrac{p_u}{\rho_u V_u^2 \sin^2 \sigma}\right]}{\left[\left(\dfrac{\gamma - 1}{\gamma + 1}\right) + \left(\dfrac{2\gamma}{\gamma + 1}\right)\dfrac{p_u}{\rho_u V_u^2 \sin^2 \sigma}\right]^2} \tag{A8}$$

$$\frac{\partial \theta}{\partial \rho_u} = \sin^2 \theta \tan \sigma \frac{\left(\frac{\gamma + 1}{2\gamma}\right) \frac{V_u^2}{p_u}}{\left(\frac{\rho_u V_u^2}{\gamma p_u} \sin^2 \sigma - 1\right)^2} \tag{A9}$$

$$\frac{\partial p}{\partial V_u} = \frac{4 \rho_u V_u \sin^2 \sigma}{\gamma + 1} \tag{A10}$$

$$\frac{\partial \rho}{\partial V_u} = \frac{\left(\frac{4\gamma}{\gamma + 1}\right) \frac{p_u}{V_u^3 \sin^2 \sigma}}{\left[\left(\frac{\gamma - 1}{\gamma + 1}\right) + \left(\frac{2\gamma}{\gamma + 1}\right) \frac{p_u}{\rho_u V_u^2 \sin^2 \sigma}\right]^2} \tag{A11}$$

$$\frac{\partial \theta}{\partial V_u} = \sin^2 \theta \tan \sigma \frac{\left(\frac{\gamma + 1}{\gamma}\right) \frac{\rho_u V_u}{p_u}}{\left(\frac{\rho_u V_u^2}{\gamma p_u} \sin^2 \sigma - 1\right)^2} \tag{A12}$$

$$\frac{\partial p}{\partial \zeta_u} = \frac{\partial p}{\partial \sigma} = \frac{4 \rho_u}{\gamma + 1} V_u^2 \sin \sigma \cos \sigma \tag{A13}$$

$$\frac{\partial \rho}{\partial \zeta_u} = \frac{\partial \rho}{\partial \sigma} = 2 \rho_d \left[\cot \sigma - \frac{\sin \sigma \cos \sigma}{\sin^2 \sigma + \left(\frac{2\gamma}{\gamma - 1}\right) \frac{p_u}{\rho_u V_u^2}} \right] \tag{A14}$$

$$\frac{\partial \theta}{\partial \zeta_u} = \frac{\partial \theta}{\partial \sigma} = 1 - \frac{\sin(\sigma - \theta)\cos(\sigma - \theta)}{\sin \sigma \cos \sigma} + \frac{4\gamma p_u \cos^2(\sigma - \theta)}{(\gamma + 1)\rho_u V_u^2 \sin^2 \sigma} \tag{A15}$$

For a real gas in equilibrium, the shock conditions are implicit (i.e., they must be obtained by iteration), therefore the derivatives above must be evaluated numerically. Although the results of flow-field calculations presented herein are for thermally perfect air, it is instructive to compare equations (A4) to (A12) with the results of numerical calculations for dissociated

air. This comparison is made in figure 10 as a function of the upstream velocity normal to the shock. The gas properties used in the calculations were obtained from curve fits to equilibrium thermodynamic properties generated in the manner described in reference 17.

Gradients of the Zero Incidence Flow Field

The derivatives of flow variables along streamlines and normal to the streamlines play an important part in the calculation of the perturbation flow field. For the usual mesh point, a simple linear backward difference method is used for evaluating these derivatives. This method is not well suited, however, for calculating the downstream gradients along the bow shock, and especially along an embedded shock. For these cases, a more accurate method is used which makes use of the differential equations of motion directly. These are written in terms of streamline coordinates (see, e.g., Hayes and Probstein, ref. 18)

$$\frac{\beta^2}{\rho V^2}\frac{\partial p}{\partial s} = -\frac{\partial \theta}{\partial n} - \epsilon\frac{\sin\theta}{r} \tag{A16}$$

$$\frac{1}{\rho V^2}\frac{\partial p}{\partial n} = -\frac{\partial \theta}{\partial s} \tag{A17}$$

where $\epsilon = 0$ for two-dimensional flow

$\epsilon = 1$ for axisymmetric three-dimensional flow

and s, n are distances along and normal to the streamline. The vector gradients of p and θ along the shock wave may be written in terms of components along the s, n coordinates in the following way (see sketch (e))

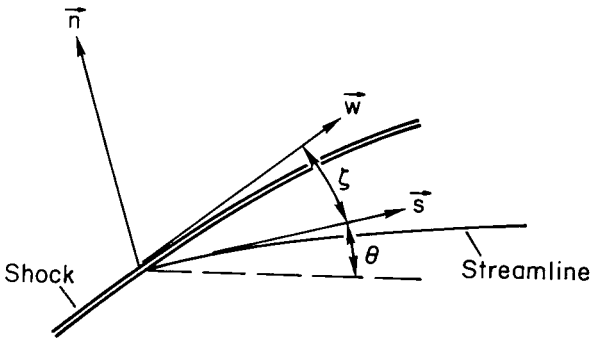

Sketch (e)

$$\frac{\partial p}{\partial W} = \cos\zeta\frac{\partial p}{\partial s} + \sin\zeta\frac{\partial p}{\partial n} \tag{A18}$$

$$\frac{\partial \theta}{\partial W} = \cos\zeta\frac{\partial \theta}{\partial s} + \sin\zeta\frac{\partial \theta}{\partial n} \tag{A19}$$

Equations (A16) to (A19) contain four unknown derivatives of p and θ with respect to s and n in terms of gradients along the shock. Substitution yields the following expressions for the streamline pressure gradient and the streamline curvature:

$$\frac{\partial p}{\partial s} = \frac{\left(\frac{\partial p}{\partial W}\right) \cos \zeta + \rho V^2 \sin \zeta \left(\frac{\partial \theta}{\partial W} + \epsilon \frac{\sin \theta \sin \zeta}{r}\right)}{\cos^2 \zeta - \beta^2 \sin^2 \zeta} \tag{A20}$$

$$\frac{\partial \theta}{\partial s} = \frac{\frac{\beta^2}{\rho V^2} \frac{\partial p}{\partial W} \sin \zeta + \cos \zeta \left(\frac{\partial \theta}{\partial W} + \epsilon \frac{\sin \theta \sin \zeta}{r}\right)}{\cos^2 \zeta - \beta^2 \sin^2 \zeta} \tag{A21}$$

The remaining derivatives can then be found from equations (A16) and (A17). The entropy gradient can also be expressed in terms of the gradient along the shock. In this case, since the entropy is constant on streamlines, one obtains

$$\frac{dS}{dn} = \frac{1}{\sin \zeta} \frac{dS}{dW} \tag{A22}$$

Equations (A20) and (A21) require derivatives of p, θ, and ρ along the shock wave, evaluated on the downstream side. These can be obtained in terms of the upstream gradients, which are presumed known, by means of the shock derivatives (A3); that is

$$\frac{\partial p}{\partial W} = \sum_{k=1}^{4} \frac{\partial p}{\partial g_k} \frac{\partial g_k}{\partial W} \tag{A23}$$

$$\frac{\partial \theta}{\partial W} = \sum_{k=1}^{4} \frac{\partial \theta}{\partial g_k} \frac{\partial g_k}{\partial W} \tag{A24}$$

where the derivatives $\partial g_k/\partial W$ are determined from the upstream gradients.

Equation (A23) contains the shock curvature, $\partial\sigma/\partial W$, which enters through the derivative of ζ_u

$$\frac{\partial \zeta_u}{\partial W} = \frac{\partial \sigma}{\partial W} - \frac{\partial \theta_u}{\partial W}$$

For a general shock point the shock curvature is found by a linear difference. Near a corner, however, this quantity is evaluated differently as described next.

Shock-Wave Curvature

When a nonuniform supersonic stream flows over a compression corner, the initial shock angle at the corner is equal to the two-dimensional oblique shock value, and the shock will have a finite curvature even though the body may be straight. On the other hand, a curved body will produce a curved shock in a uniform stream. The latter problem has been considered by a number of authors (see, e.g., ref. 19). In either case, the initial shock curvature can be evaluated from the equations given in this appendix. The shock curvature depends on the streamline curvature downstream of the shock which is determined from a knowledge of the body shape. Equations (A23) and (A24) can be used in conjunction with equation (A21) for the streamline curvature in evaluating the shock-wave curvature. First, however, it will be convenient to rewrite equations (A23) and (A24) in the form

$$\frac{\partial p}{\partial W} = K_p + \frac{\partial p}{\partial \sigma} K_W \tag{A25}$$

$$\frac{\partial \theta}{\partial W} = K_\theta + \frac{\partial \theta}{\partial \sigma} K_W \tag{A26}$$

where

$$K_P = \frac{\partial p}{\partial p_u}\frac{\partial p_u}{\partial W} + \frac{\partial p}{\partial \rho_u}\frac{\partial \rho_u}{\partial W} + \frac{\partial p}{\partial V_u}\frac{\partial V_u}{\partial W} - \frac{\partial p}{\partial \sigma}\frac{\partial \theta_u}{\partial W}$$

$$K_\theta = \frac{\partial \theta}{\partial p_u}\frac{\partial p_u}{\partial W} + \frac{\partial \theta}{\partial \rho_u}\frac{\partial \rho_u}{\partial W} + \frac{\partial \theta}{\partial V_u}\frac{\partial V_u}{\partial W} - \left(\frac{\partial \theta}{\partial \sigma} - 1\right)\frac{\partial \theta_u}{\partial W}$$

and where

$$K_W = \frac{\partial \sigma}{\partial W}$$

is the shock-wave curvature. The terms K_P and K_θ represent the gradients along a straight shock wave, and the remaining term represents the gradient due to shock curvature. Substitution of equations (A25) and (A26) into (A21) yields, after some rearranging

$$K_W = -\frac{K_B(\cos^2 \zeta - \beta^2 \sin^2 \zeta) - \cos \zeta\left[\left(\frac{\beta^2}{\rho V^2}\right) K_p \tan \zeta + K_\theta + \frac{\epsilon}{r} \sin \theta \sin \zeta\right]}{\frac{\beta^2}{\rho V^2}\frac{\partial p}{\partial \sigma} \sin \zeta + \frac{\partial \theta}{\partial \sigma} \cos \zeta} \tag{A27}$$

where

$$K_B = \frac{\partial \theta}{\partial s}$$

is the body surface curvature behind the shock. This expression depends on the body curvature, on the flow-field gradients upstream of the shock, and on the derivatives of the shock-wave equations. These conditions are known from the solution of the flow upstream of the corner. The initial shock curvature for a two-dimensional or axisymmetric flare in a nonuniform stream is therefore determined.

REFERENCES

1. Seiff, Alvin: Secondary Flow Fields Embedded in Hypersonic Shock Layers. NASA TN D-1304, 1962.

2. Jorgensen, Leland H.; and Graham, Lawrence A.: Predicted and Measured Aerodynamic Characteristics for Two Types of Atmosphere-Entry Vehicles. NASA TM X-1103, 1965.

3. Seiff, Alvin; and Whiting, Ellis E.: The Effect of the Bow Shock Wave on the Stability of Blunt-Nosed Slender Bodies. NASA TM X-377, 1960.

4. Menees, Gene P.; and Smith, Willard G.: A Study of the Stability and Drag of Several Aerodynamic Shapes in Air, Carbon Dioxide, and Argon at Mach Numbers From 3 to 8. NASA TM X-950, 1964.

5. Palermo, D. A.: Equations for the Hypersonic Flow Field of the Polaris Re-Entry Body. LMSD-480954, Lockheed Missiles and Space Division, Lockheed Aircraft Corp., Oct. 1960.

6. Inouye, Mamoru; Rakich, John; and Lomax, Harvard: A Description of Numerical Methods and Computer Programs for Two-Dimensional and Axisymmetric Supersonic Flow Over Blunt-Nosed and Flared Bodies. NASA TN D-2970, 1965.

7. Rakich, John V.: Numerical Calculation of Supersonic Flows of a Perfect Gas Over Bodies of Revolution at Small Angles of Yaw. NASA TN D-2390, 1964.

8. Rakich, John V.: Calculation of Hypersonic Flow Over Bodies of Revolution at Small Angles of Attack. AIAA J., vol. 3, no. 3, Mar. 1965, pp. 458-464.

9. Ferri, Antonio: Linearized Characteristics Methods. Ch. 6, sec. G of General Theory of High Speed Aerodynamics, W. R. Sears, ed., Princeton, N. J., Princeton Univ. Press, 1954, pp. 657-668.

10. Lomax, Harvard; and Inouye, Mamoru: Numerical Analysis of Flow Properties About Blunt Bodies Moving at Supersonic Speeds in an Equilibrium Gas. NASA TR R-204, 1964.

11. Polek, Thomas E.; Holdaway, George H.; and Kemp, Joseph H., Jr.: Flow Field and Surface Pressures on a Blunt Half-Cone Entry Configuration at Mach Numbers of 7.4 and 10.4. NASA TM X-1014, 1964.

12. Crawford, D. H.: The Effect of Air Bleed on the Heat Transfer and Pressure Distribution on 30° Conical Flares at a Mach Number of 6.8. NASA TM X-439, 1961.

13. Van Dyke, M. D.: First- and Second-Order Theory of Supersonic Flow Past Bodies of Revolution. J. Aerospace Sci., vol. 18, no. 3, Mar. 1951. pp. 161-178, 216.

14. Kirk, Donn B.; and Chapman, Gary T.: Free-Flight Tests of a Blunt Nosed Flare-Stabilized Body at Speeds to 8.2 km/sec. AIAA Preprint No. 65-44, 1965.

15. Allen, H. Julian; and Perkins, Edward W.: A Study of Effects of Viscosity on Flow Over Slender Inclined Bodies of Revolution. NACA Rep. 1048, 1951. (Supersedes NACA TN 2044.)

16. Ames Research Staff: Equations, Tables, and Charts for Compressible Flow. NACA Rep. 1135, 1953.

17. Bailey, Harry E.: Equilibrium Thermodynamic Properties of Carbon Dioxide. NASA SP-3014, 1965.

18. Hayes, W. D.; and Probstein, R. F.: Hypersonic Flow Theory. Academic Press, 1959.

19. Eggers, Alfred J., Jr.; Syvertson, Clarence A.; and Kraus, Samuel: A Study of Inviscid Flow About Airfoils at High Supersonic Speeds. NACA Rep. 1123, 1953.

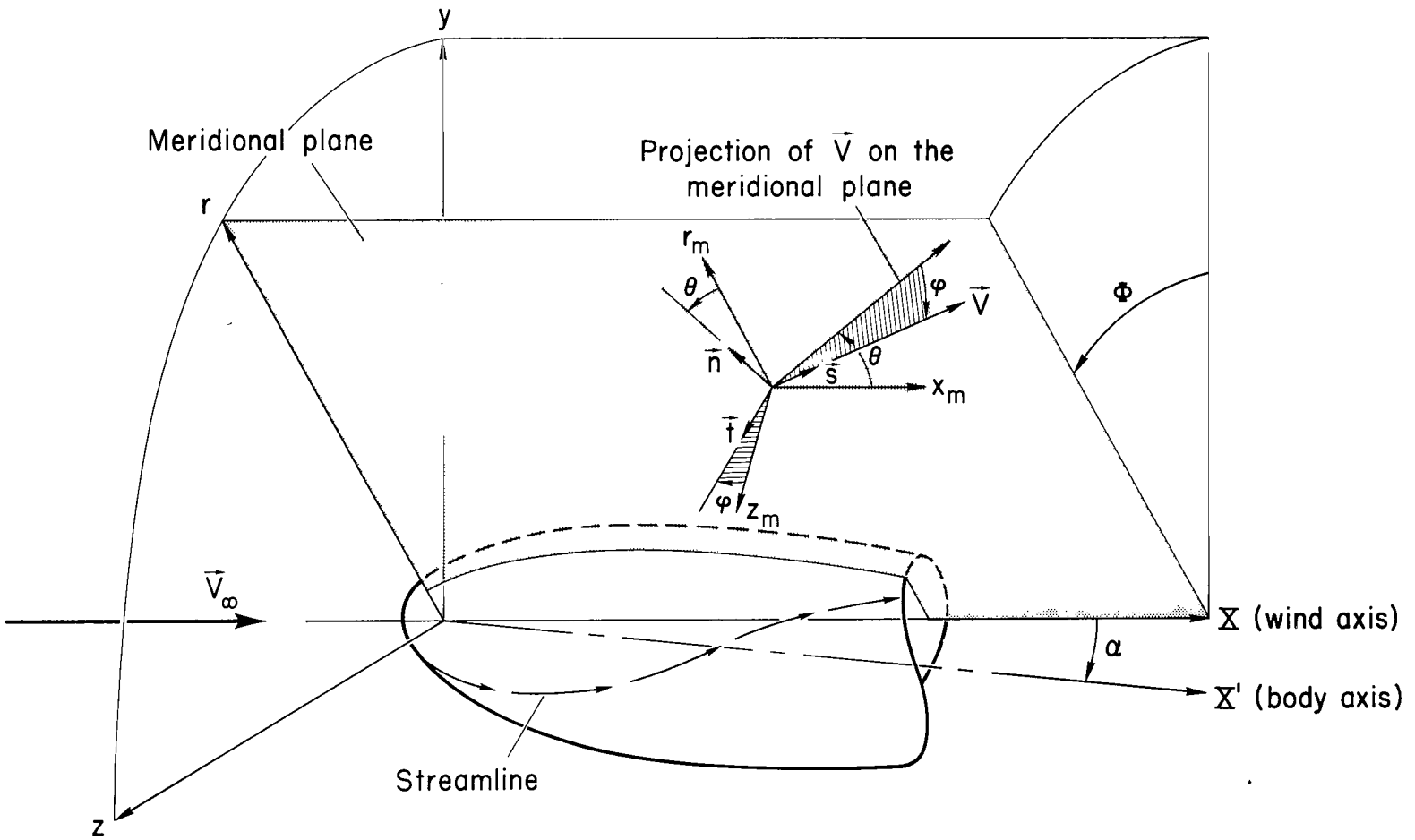

Figure 1.- Coordinate system.

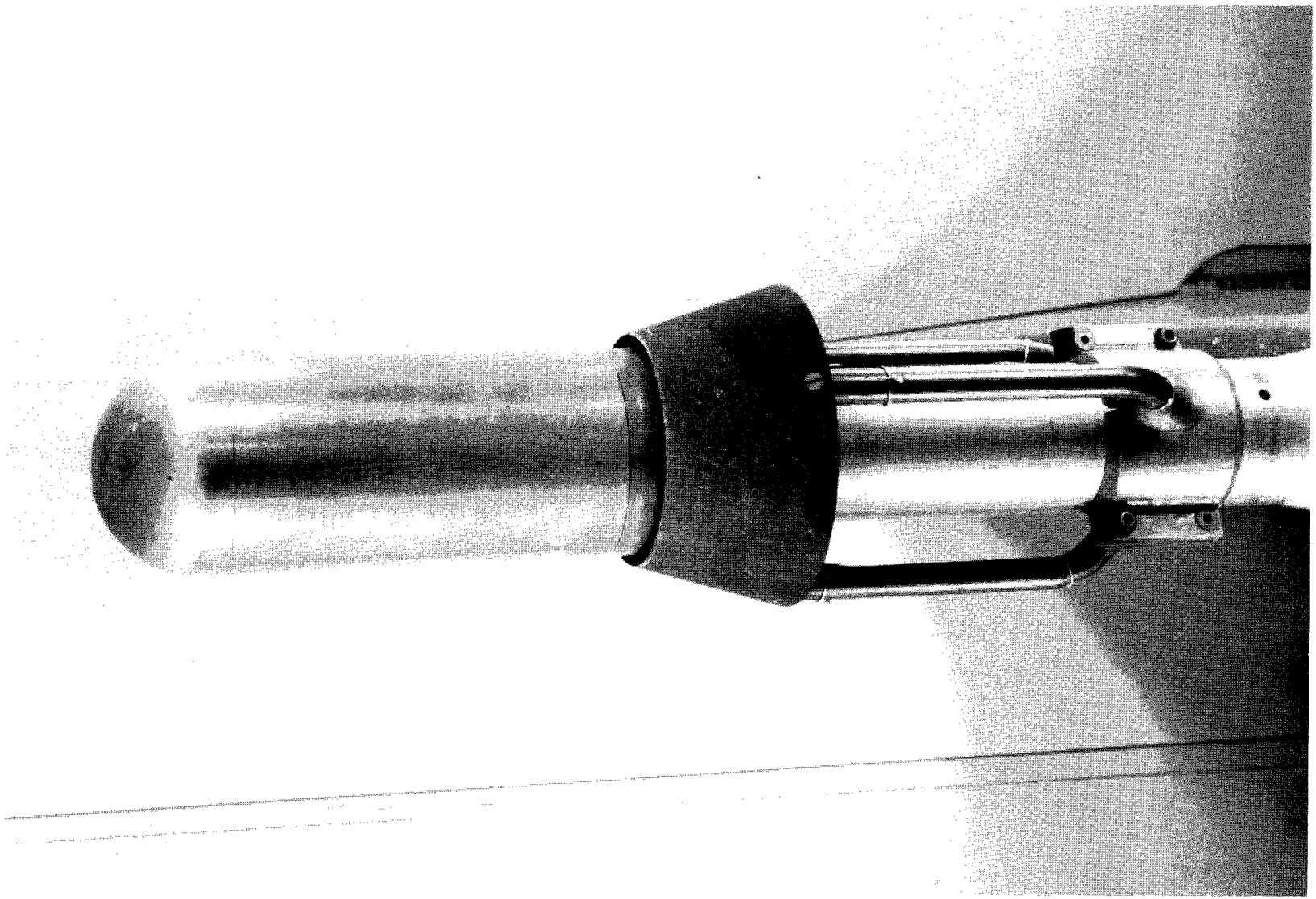

A-34709

(a) Photograph of hemispherical-nose model mounted in 3.5-foot HWT test section.

Figure 2.- Wind-tunnel models.

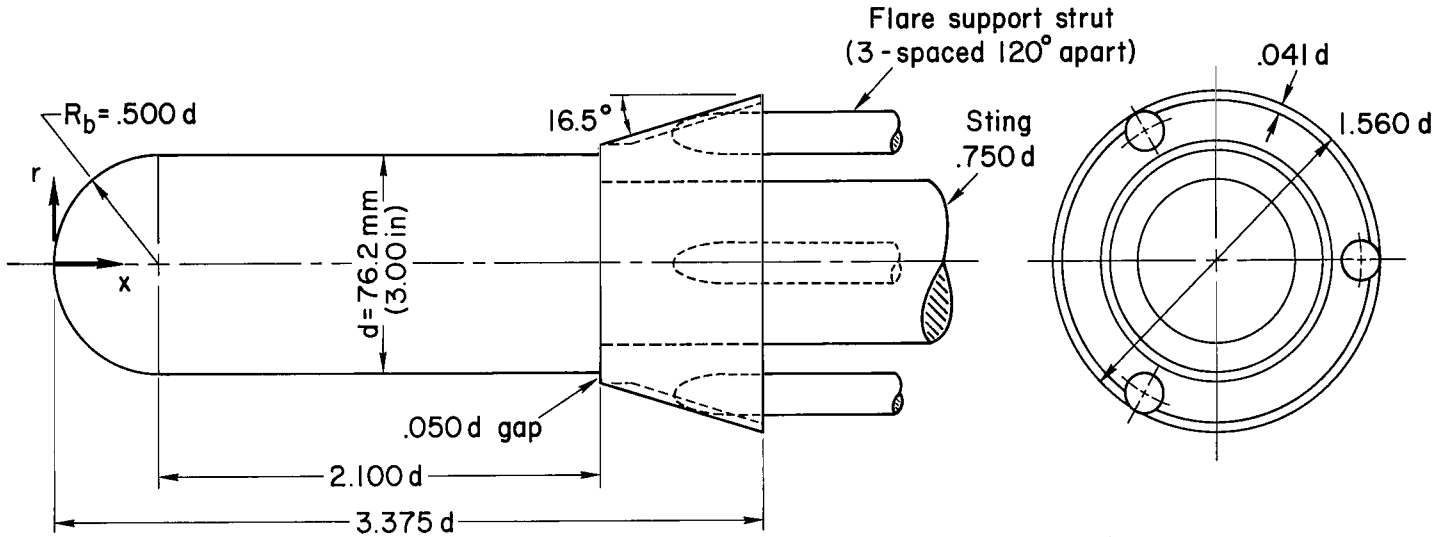

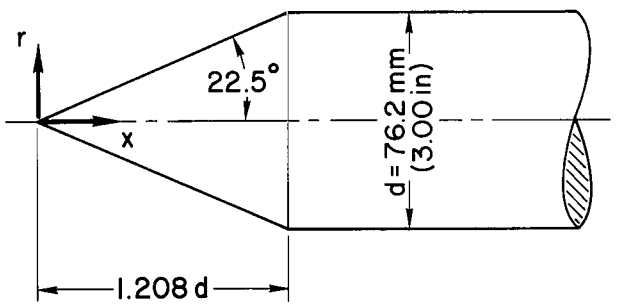

Pressure orifice locations

Hemispherical-nosed model				Conical-nosed model			
x/d	r/d	x/d	r/d	x/d	r/d	x/d	r/d
0	0	1.542	0.500	0.462	0.191	2.500	0.500
0.033	0.178	1.792	↓	.713	.295	2.750	↓
.134	.340	2.042	↓	1.022	.423	3.000	↓
.305	.460	2.292	↓	1.170	.485	3.250	↓
.457	.498	2.542	↓	1.250	.500	3.410	.530
.542	.500	2.700	.530	1.400	↓	3.570	.578
.708	↓	2.860	.577	1.584	↓	3.730	.625
.875	↓	3.020	.625	1.750	↓	3.890	.673
1.042	↓	3.180	.672	2.000	↓	4.050	.720
1.292	↓	3.340	.720	2.250	↓		

Two orifices located 180° apart at each station

(b) Dimensions.

Figure 2.- Concluded.

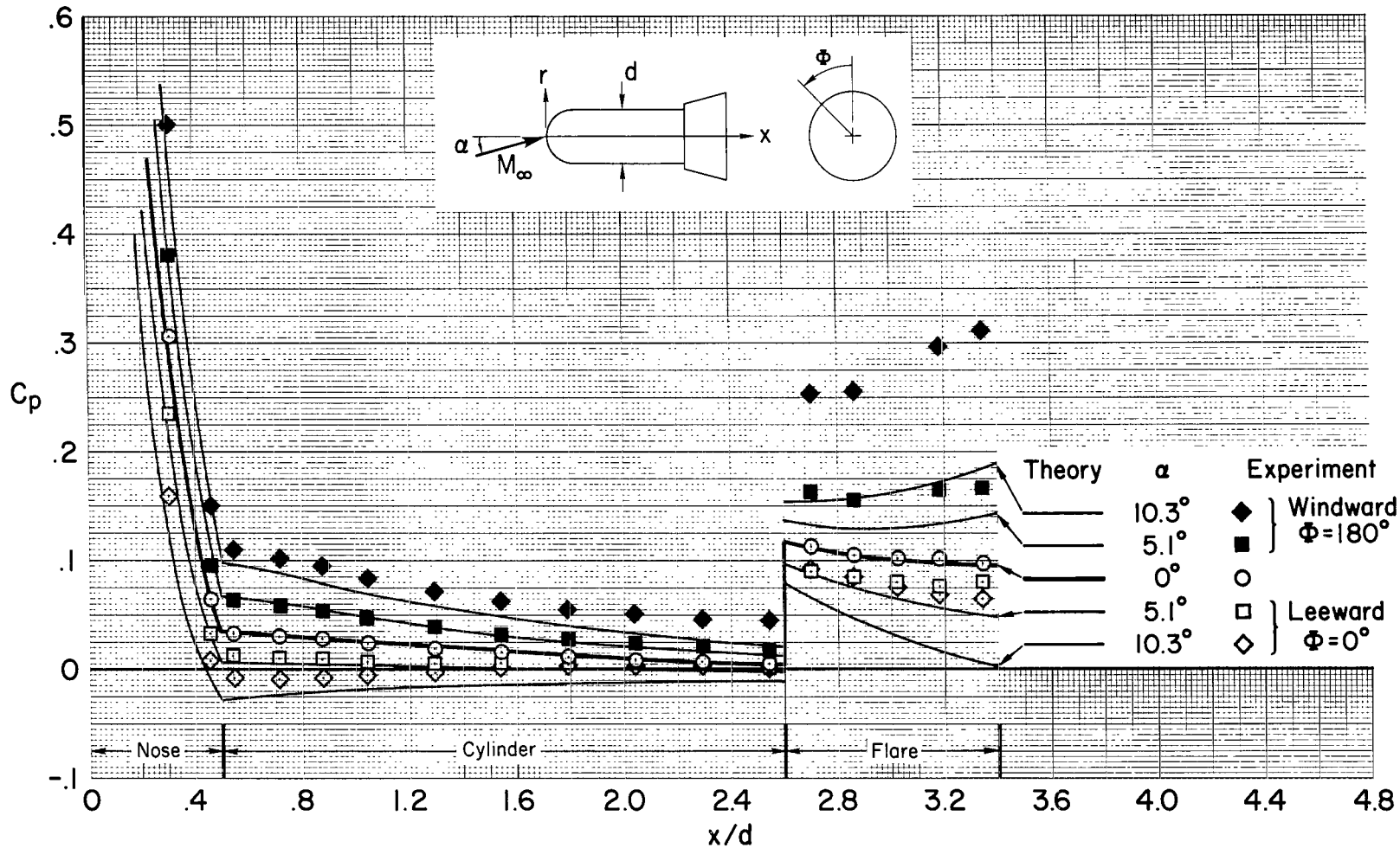

(a) $M_\infty = 5.2$

Figure 3.- Surface pressures for the hemisphere-cylinder-flare model.

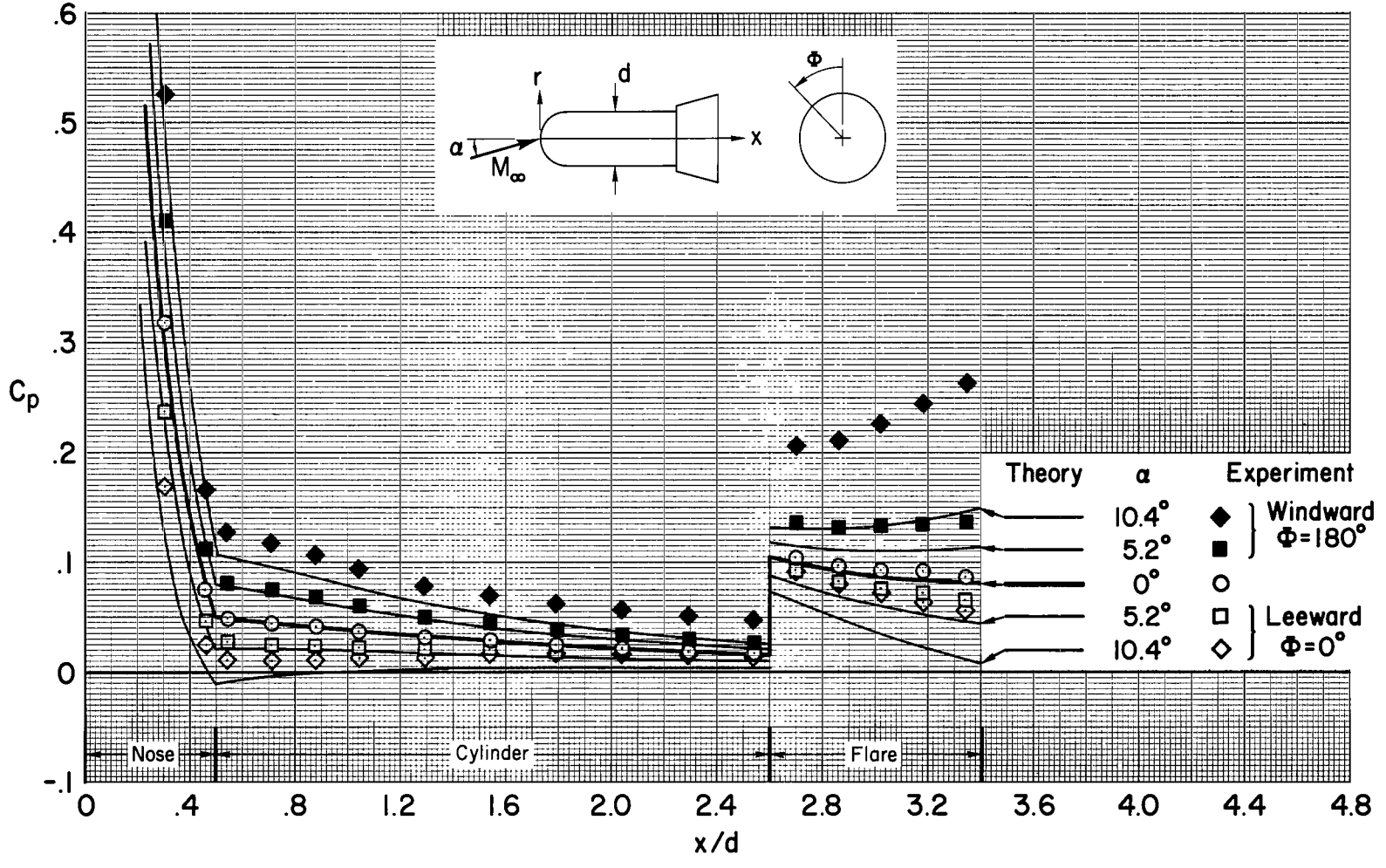

(b) $M_\infty = 7.4$

Figure 3.- Continued.

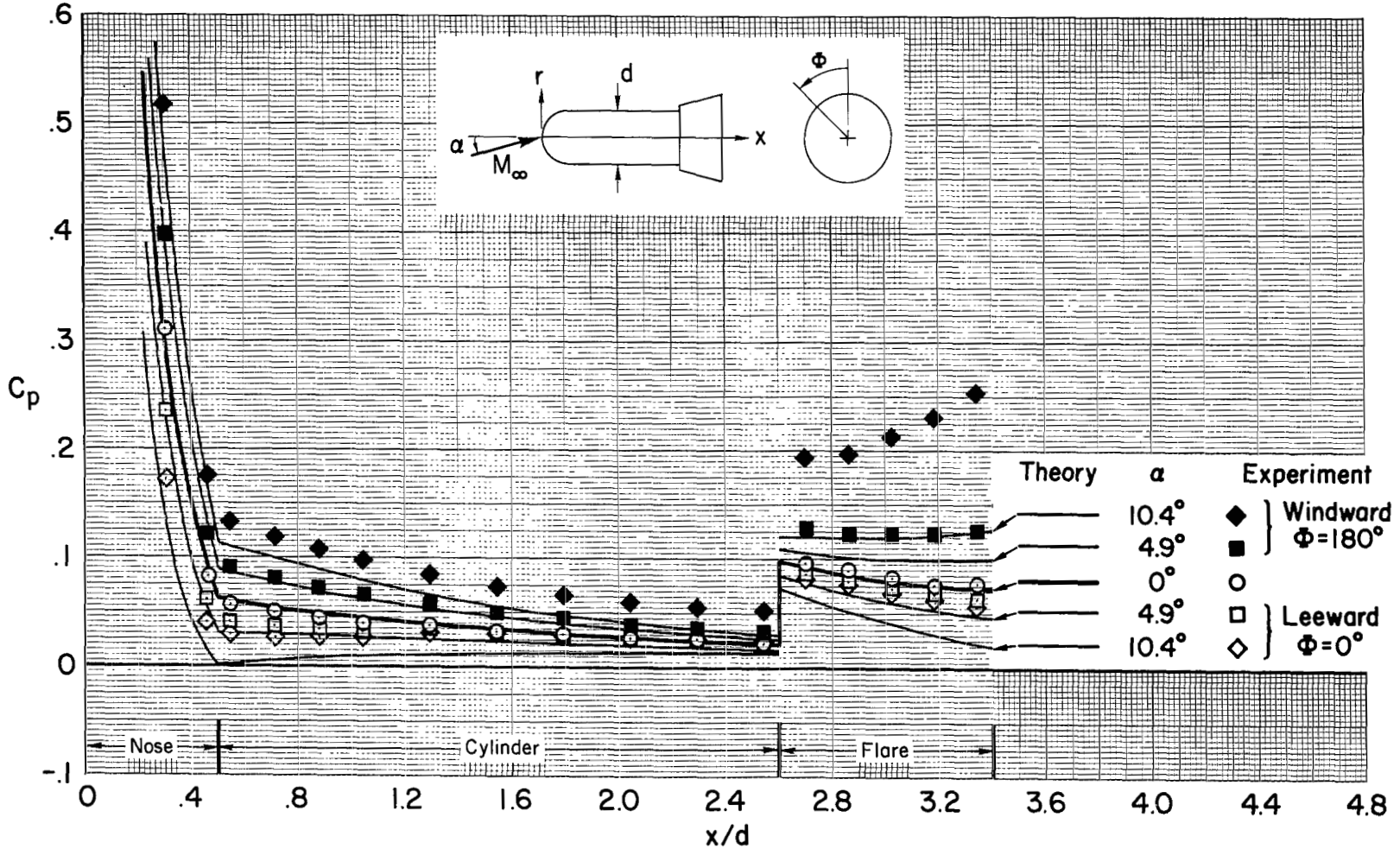

(c) M_∞ = 10.5

Figure 3.- Concluded.

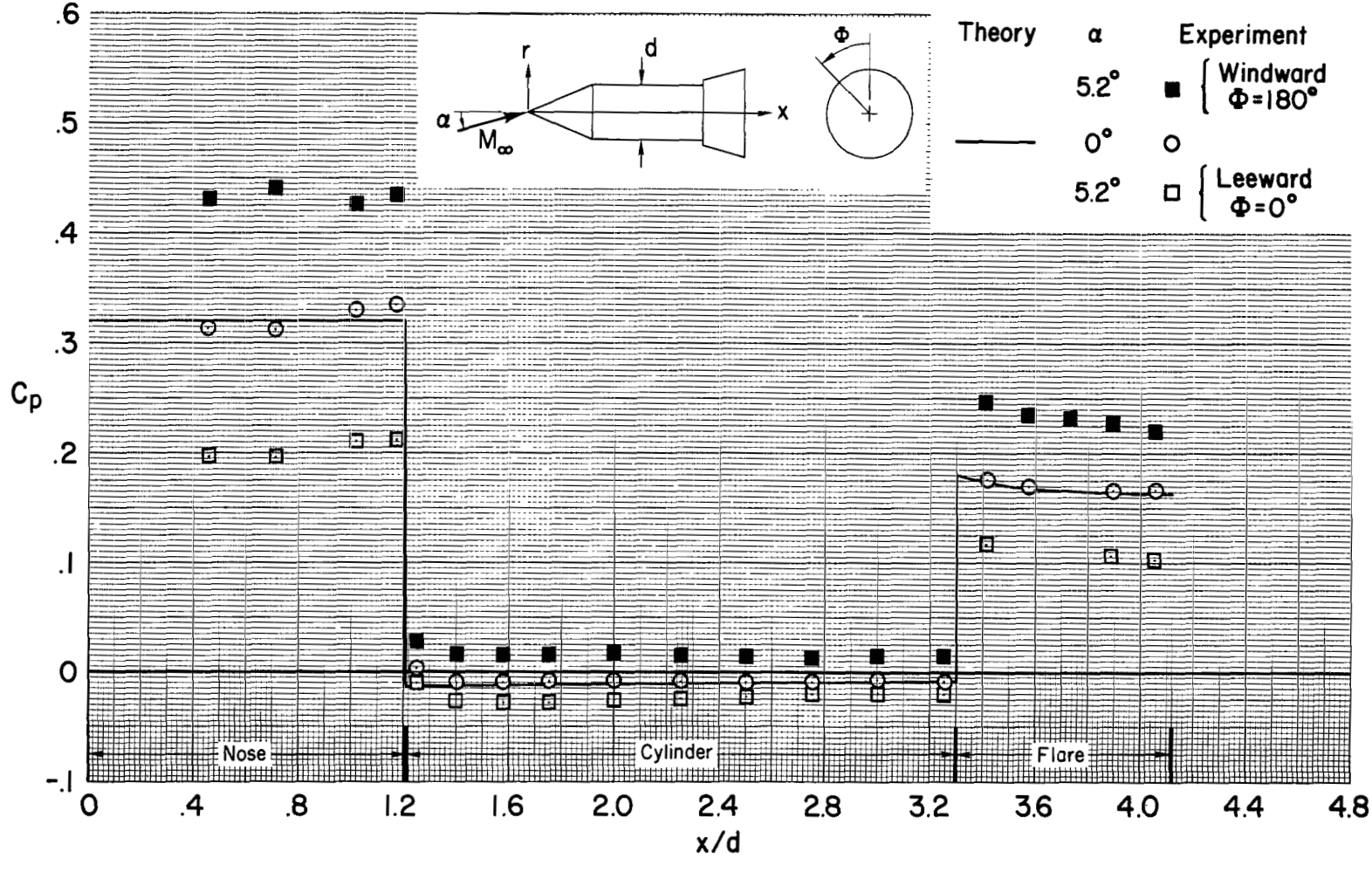

(a) $M_\infty = 5.2$

Figure 4.- Surface pressures for the cone-cylinder-flare model.

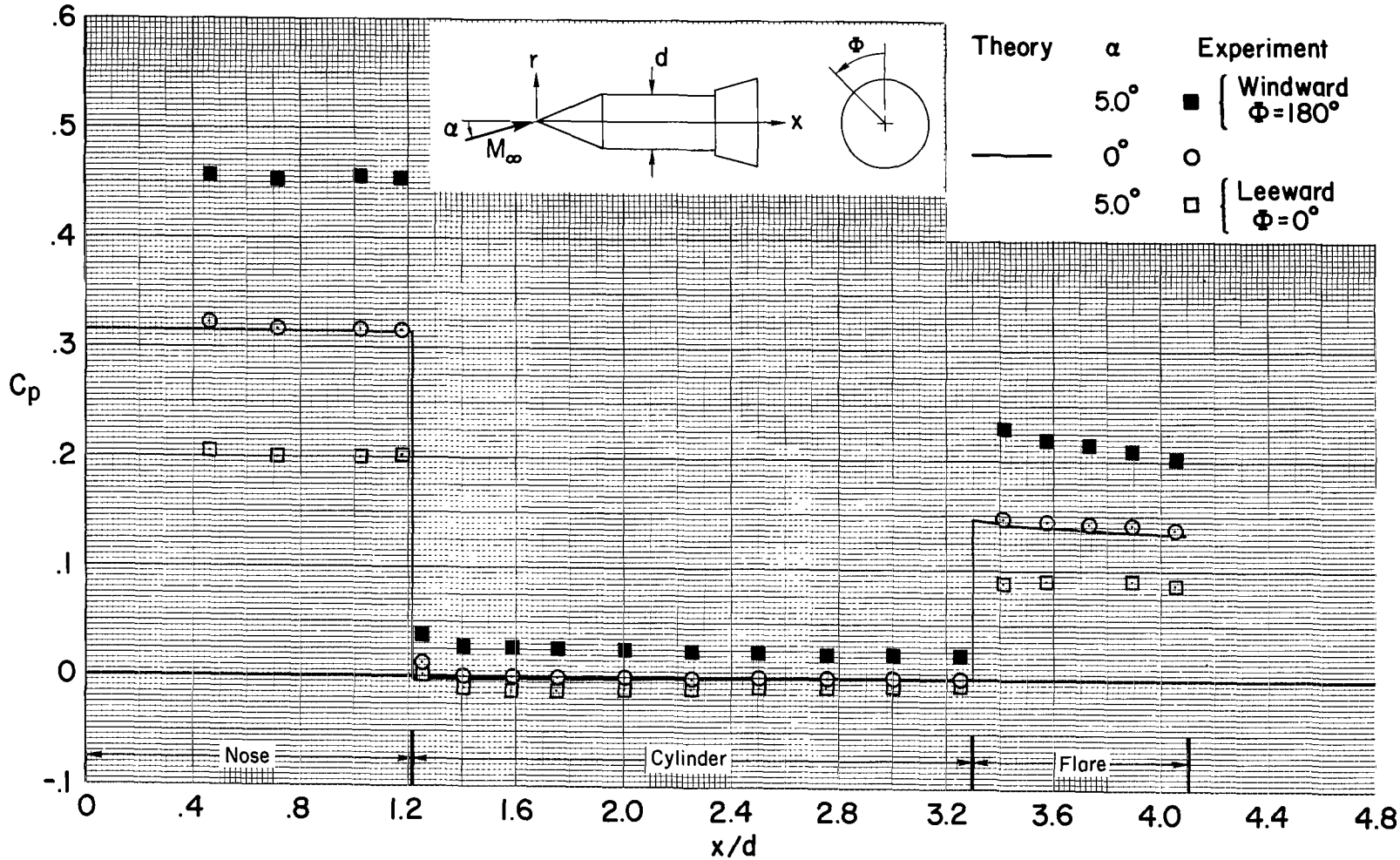

(b) $M_\infty = 7.4$

Figure 4.- Concluded.

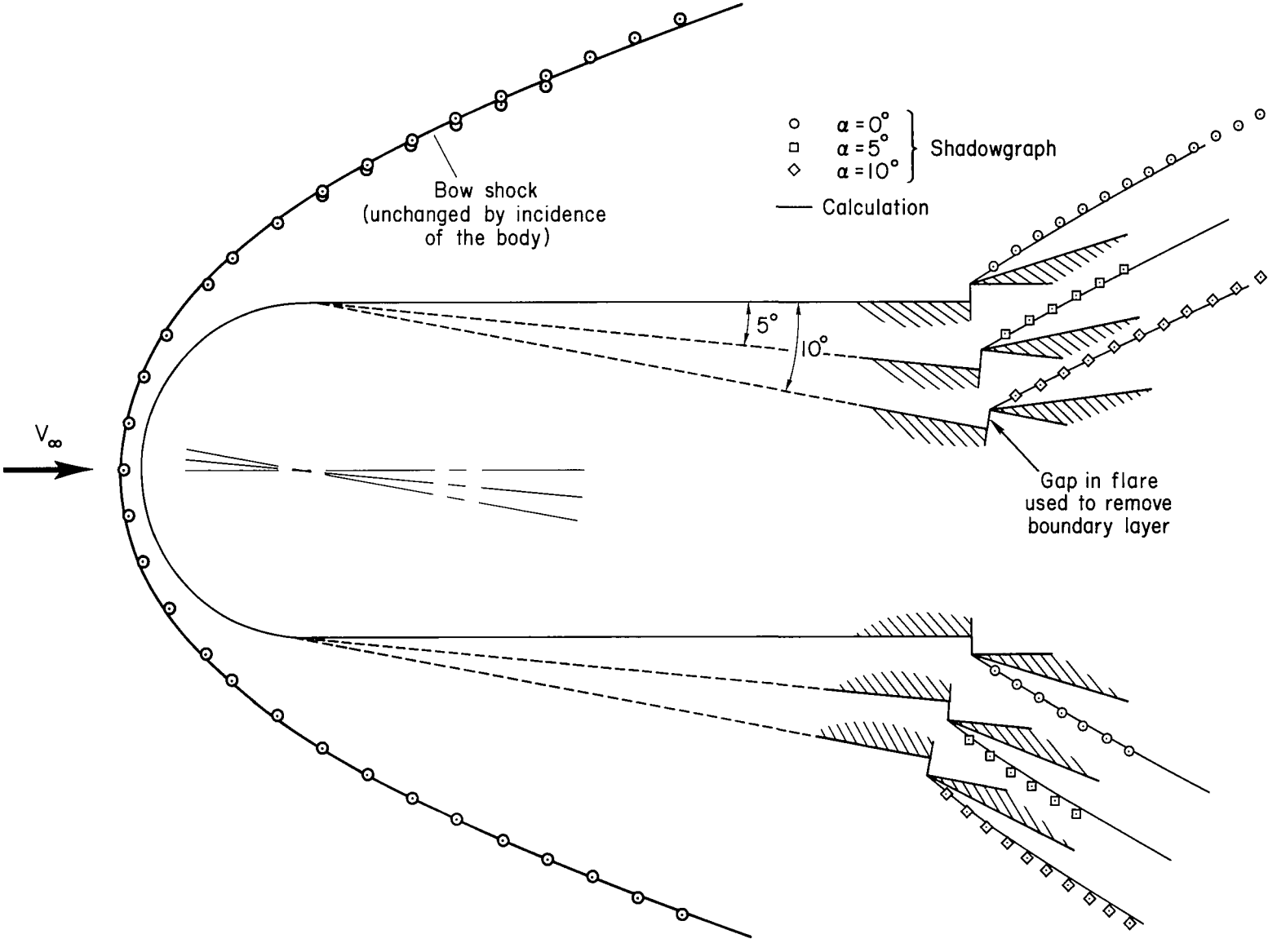

Figure 5.- Comparison of calculated and experimental shock shapes for a flared body at incidence; $M_\infty = 7.4$.

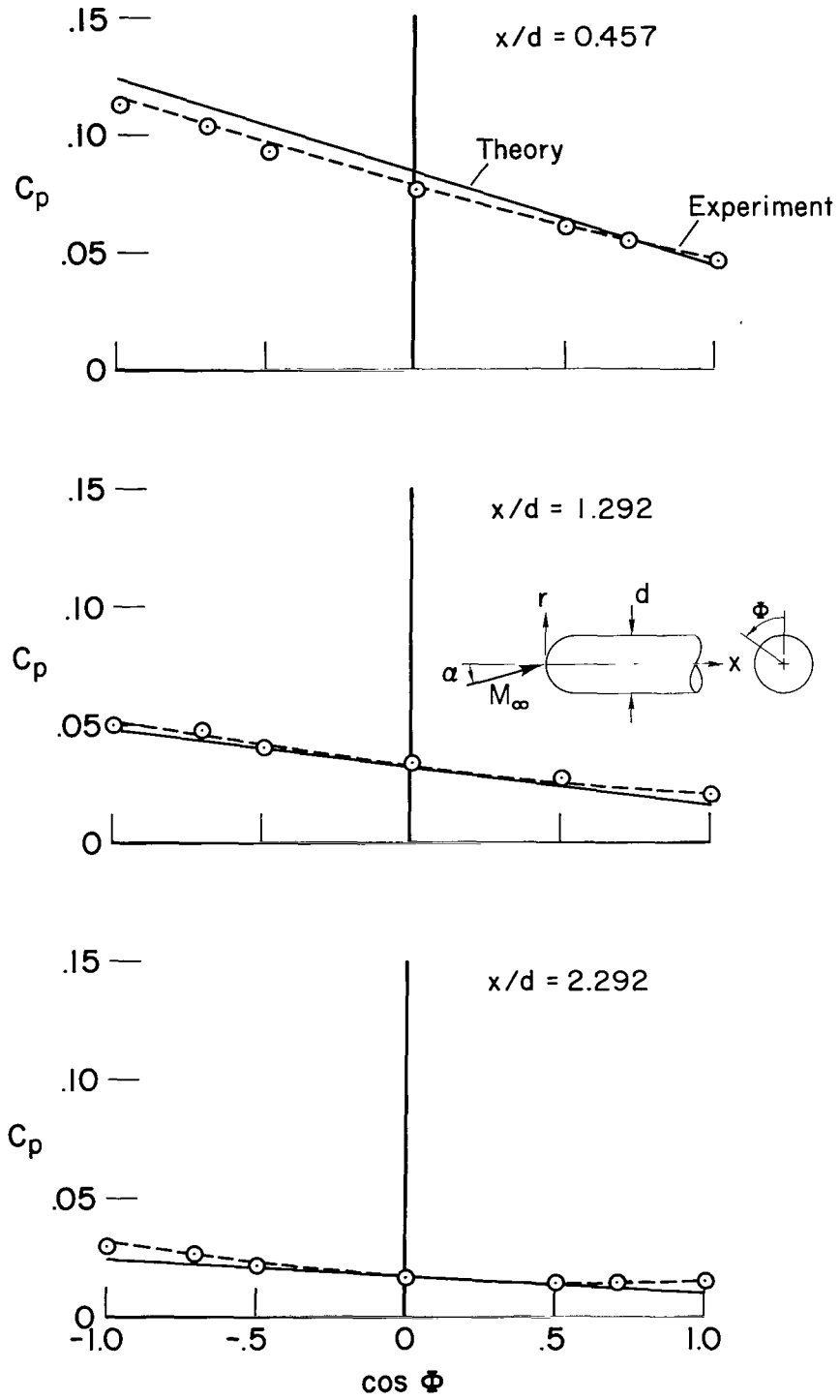

(a) $\alpha = 5^\circ$

Figure 6.- Circumferential pressure distribution for a hemisphere-cylinder; $M_\infty = 7.4$.

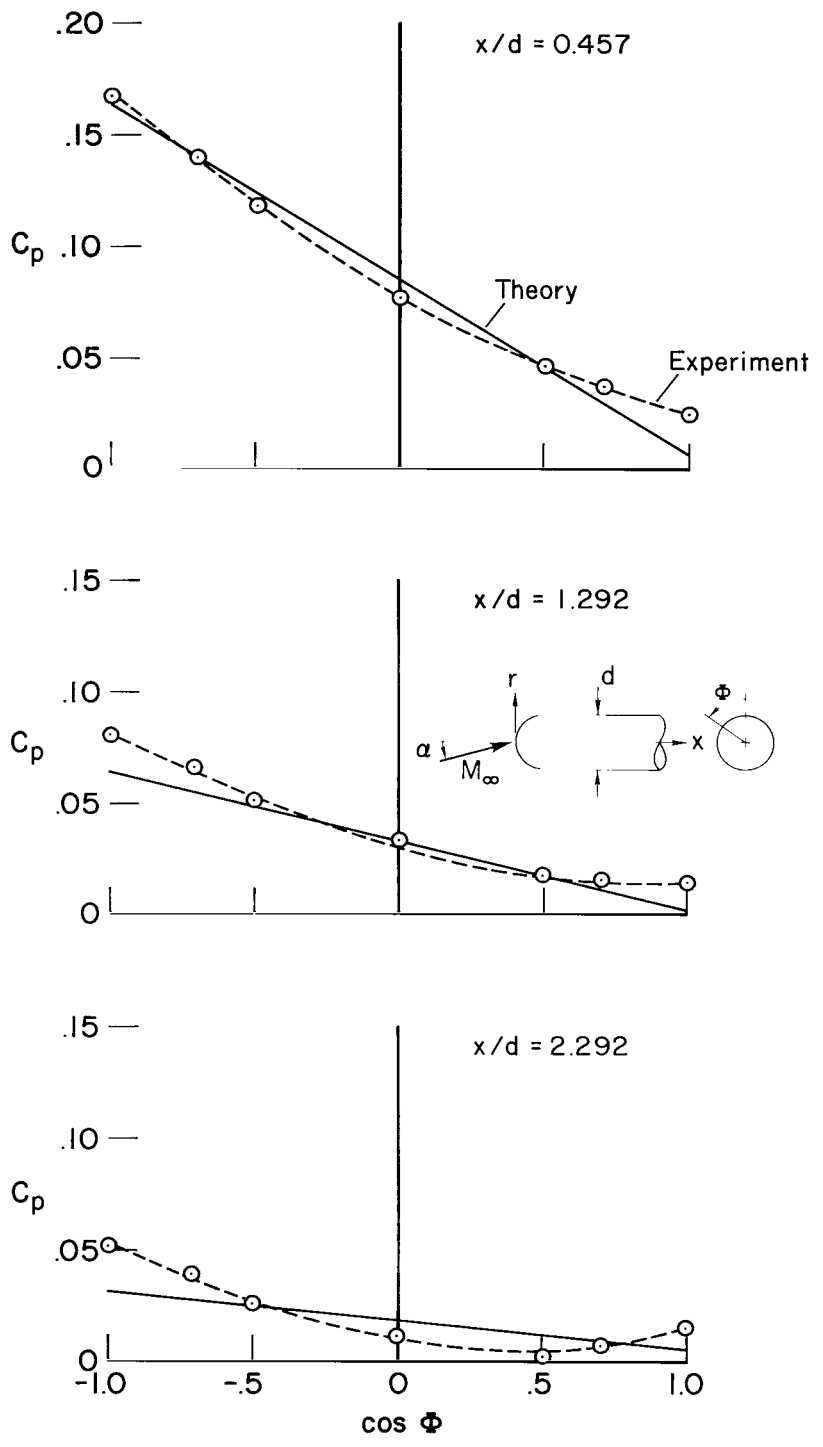

(b) $\alpha = 10^{\circ}$

Figure 6.- Concluded.

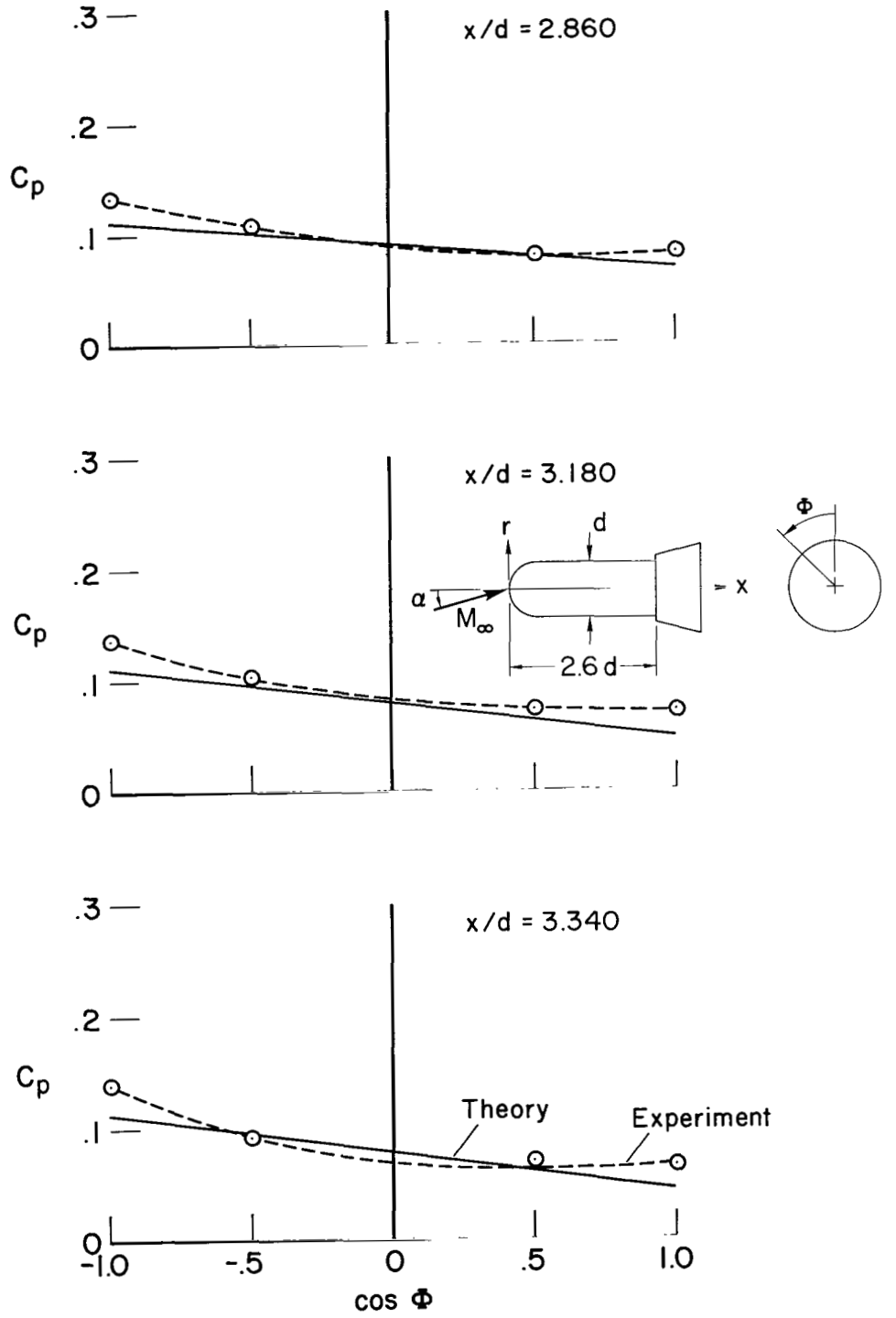

(a) $\alpha = 5^\circ$

Figure 7.- Circumferential pressure distribution for a 16.5° flare on a hemisphere-cylinder; $M_\infty = 7.4$.

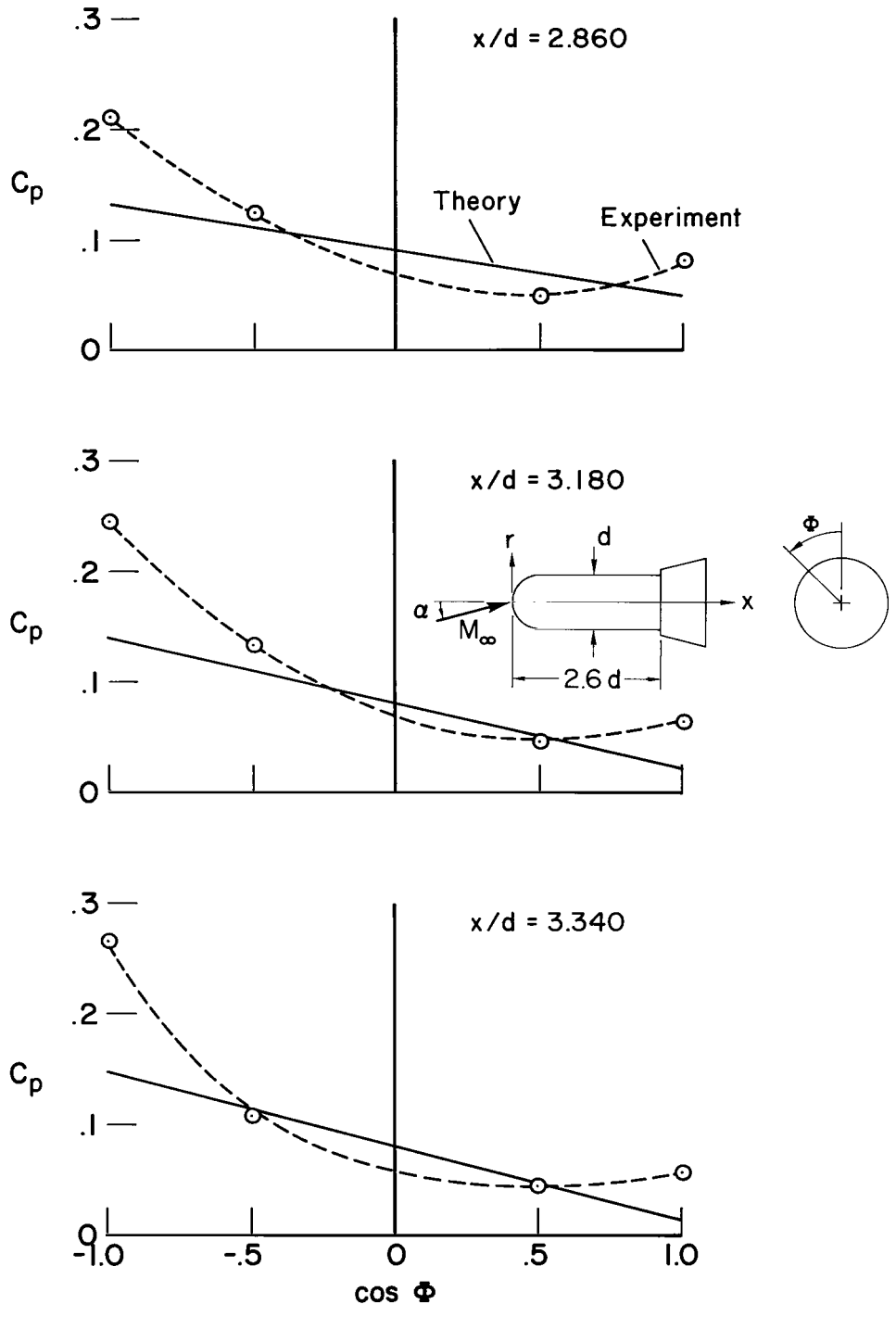

(b) $\alpha = 10^{\circ}$

Figure 7.- Concluded.

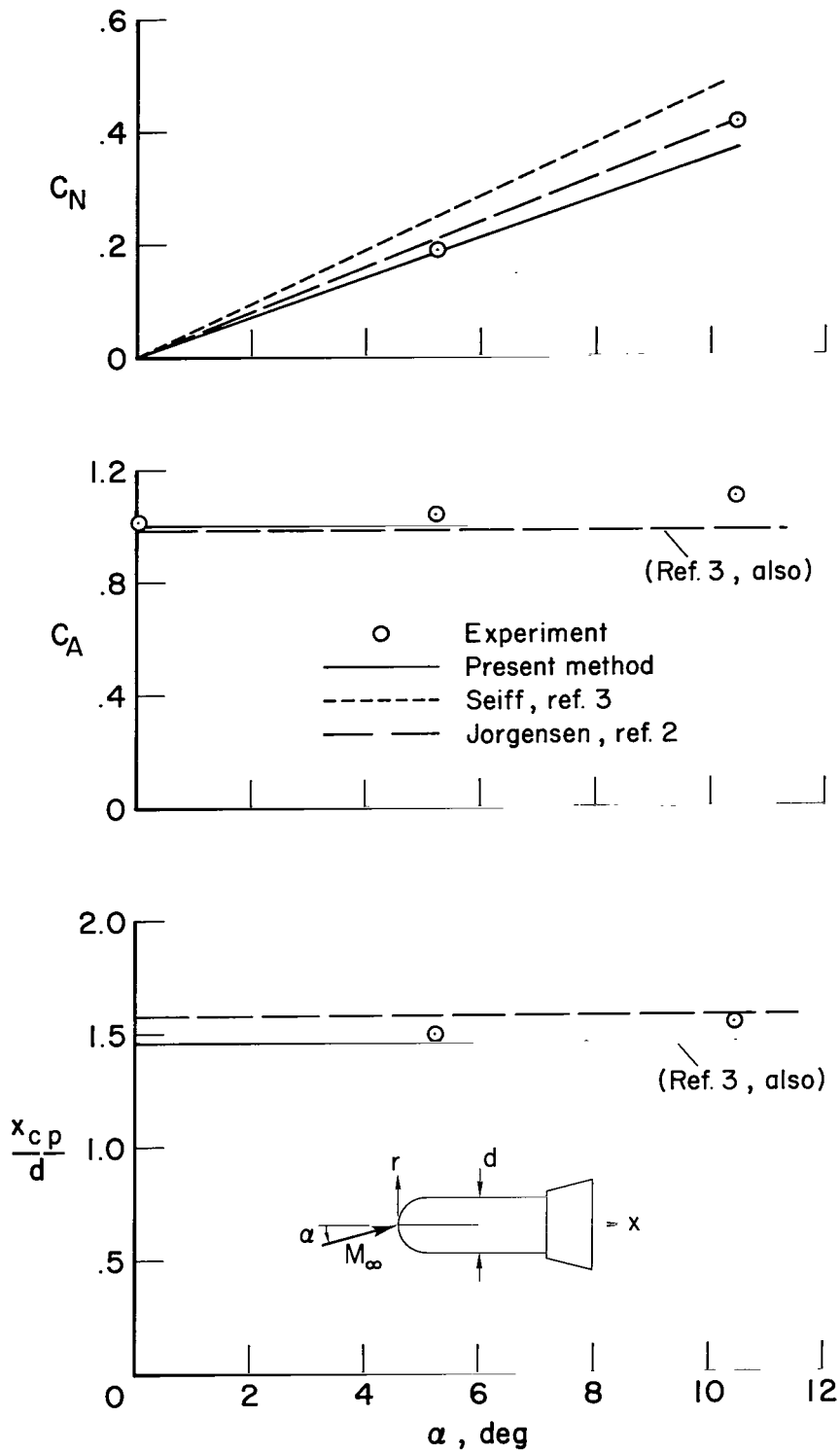

Figure 8.- Comparison of experimental and theoretical estimates of force coefficients for a hemisphere-cylinder-flare; $M_\infty = 7.4$.

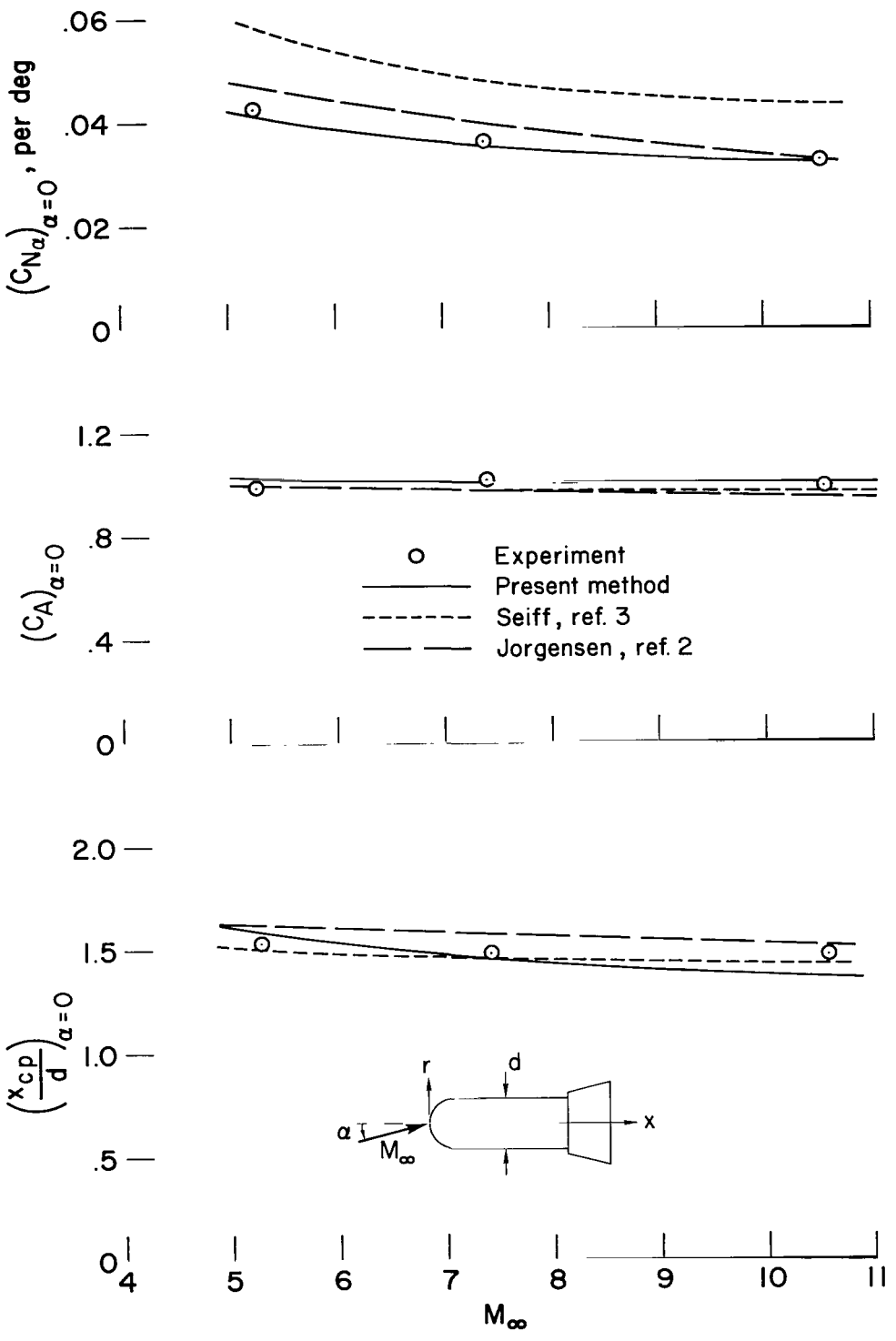

Figure 9.- Comparison of experimental and theoretical estimates of force coefficients for a hemisphere-cylinder-flare; $\alpha = 0^{\circ}$.

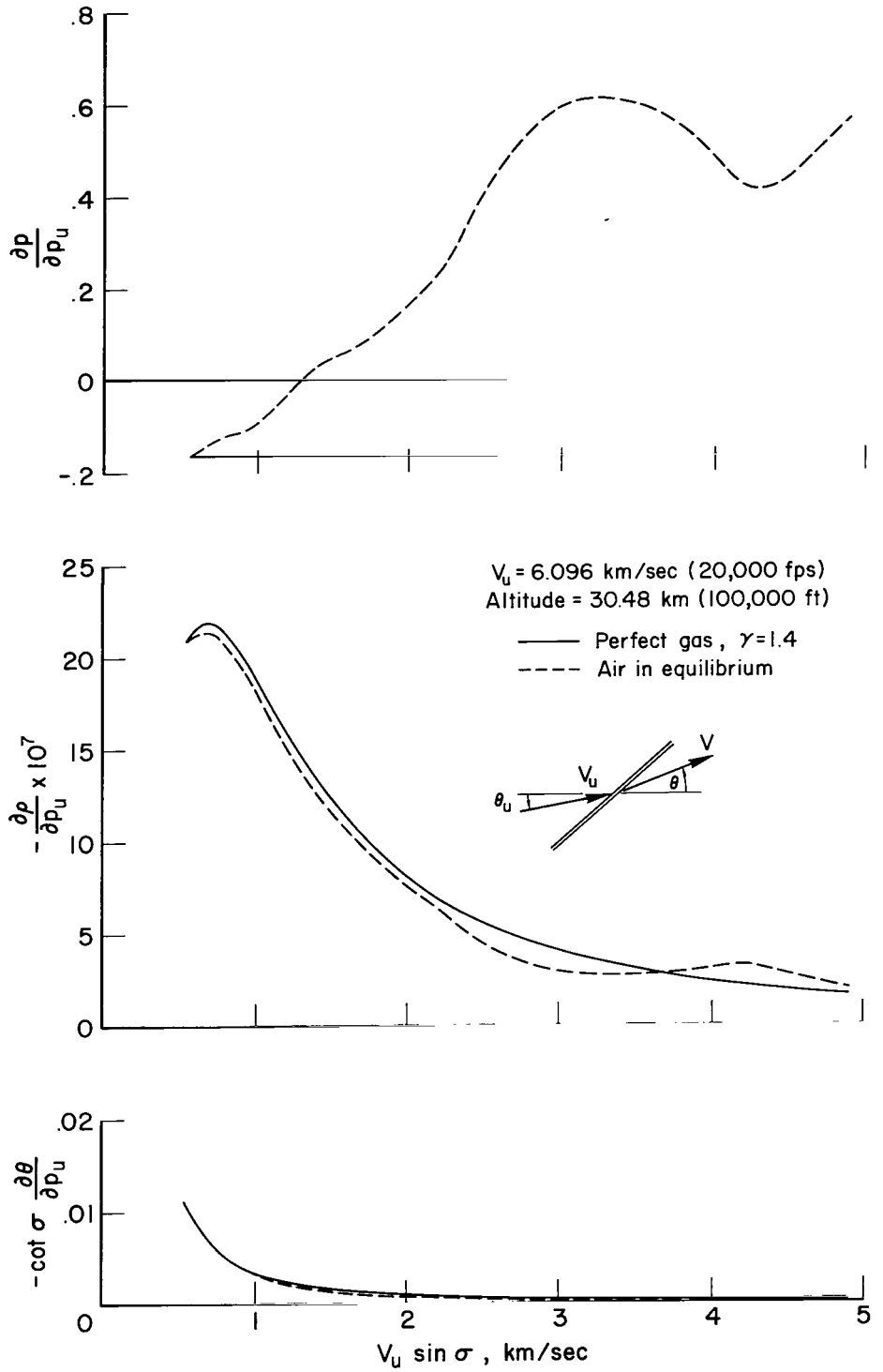

(a) Derivatives with respect to upstream pressure.

Figure 10.- Shock wave derivatives.

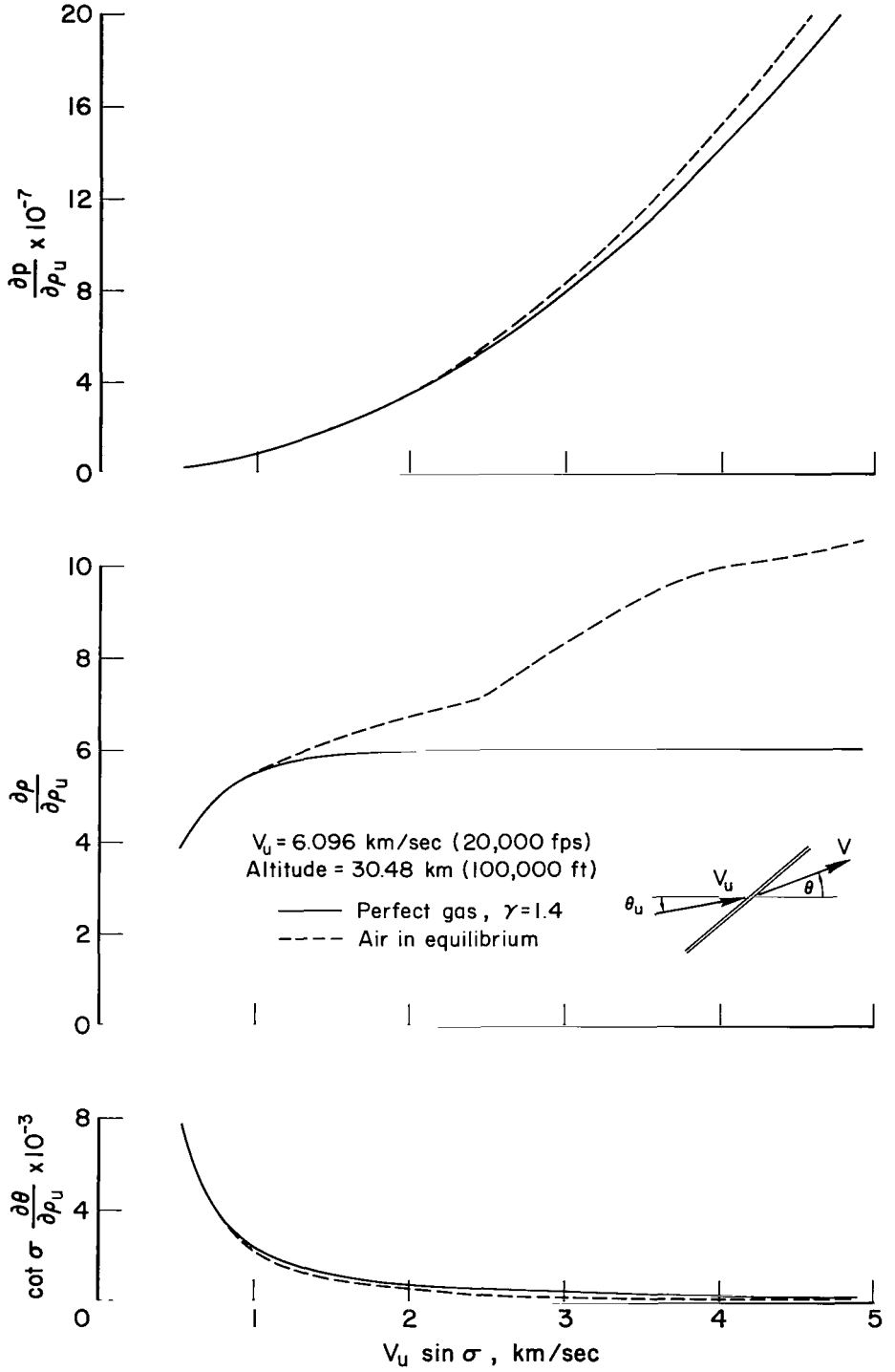

(b) Derivatives with respect to upstream density.

Figure 10.- Continued.

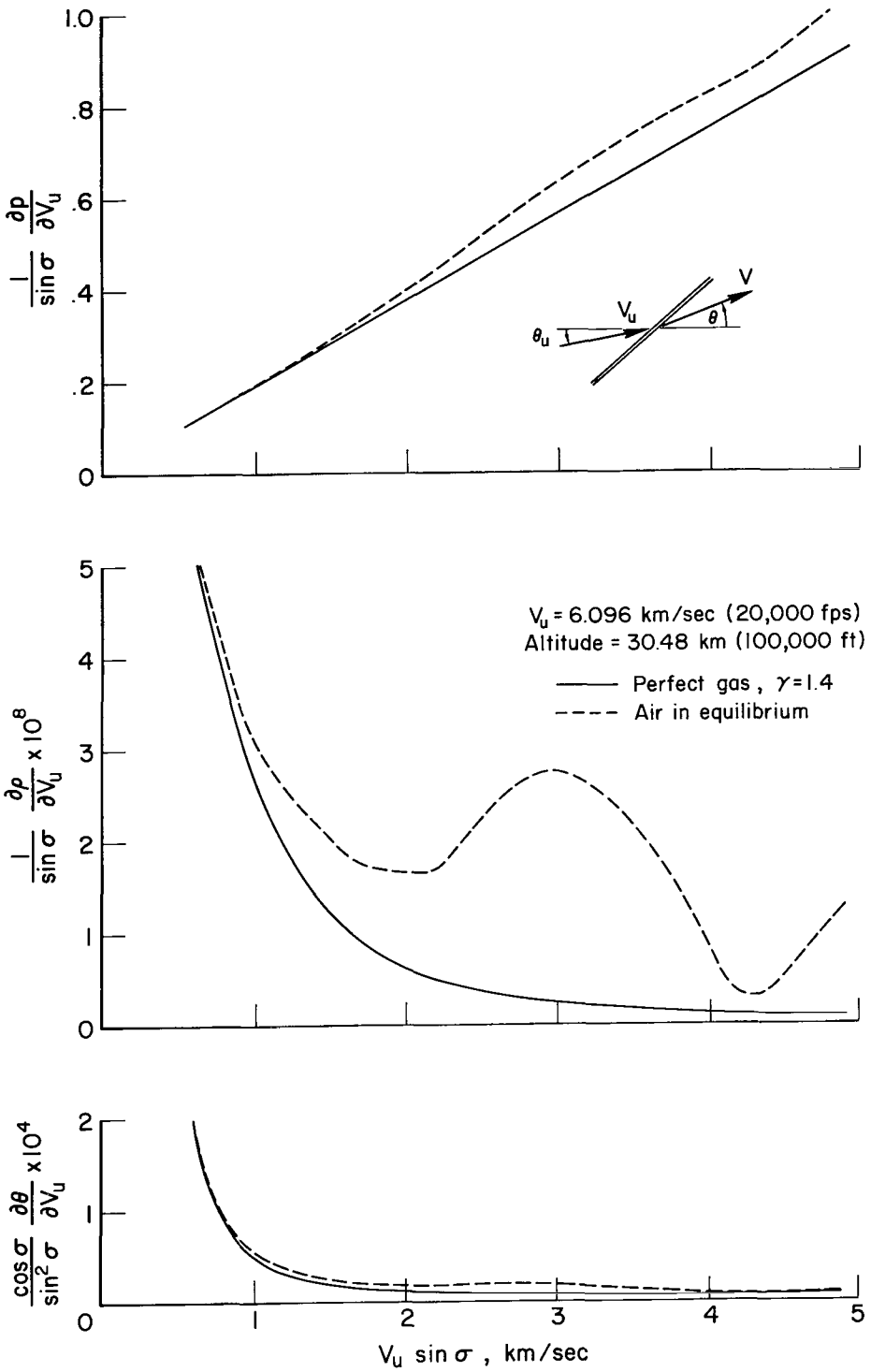

(c) Derivatives with respect to upstream velocity.

Figure 10.- Continued.

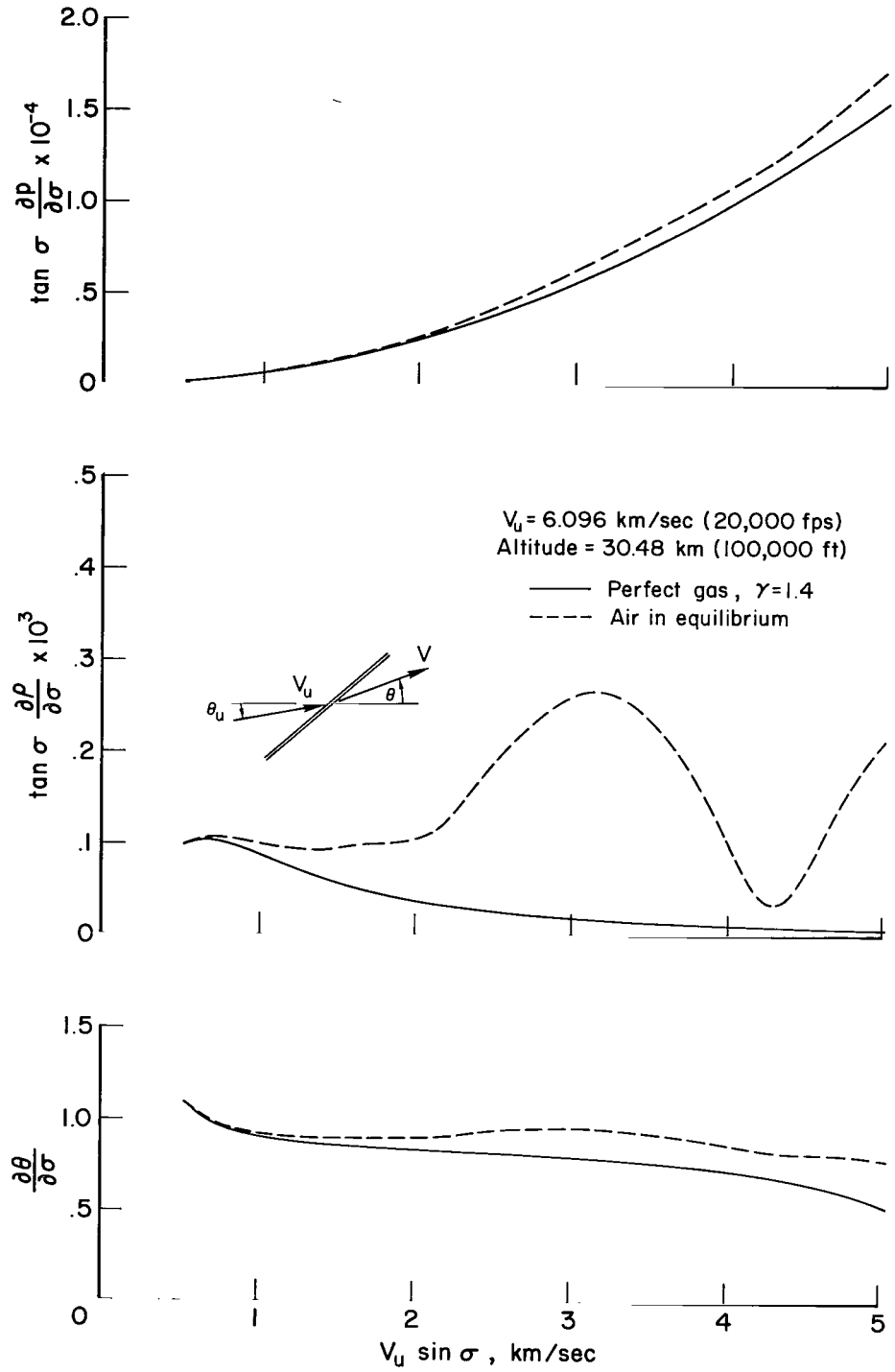

(d) Derivatives with respect to shock angle.

Figure 10.- Concluded.

"The aeronautical and space activities of the United States shall be conducted so as to contribute . . . to the expansion of human knowledge of phenomena in the atmosphere and space. The Administration shall provide for the widest practicable and appropriate dissemination of information concerning its activities and the results thereof."

—NATIONAL AERONAUTICS AND SPACE ACT OF 1958

NASA SCIENTIFIC AND TECHNICAL PUBLICATIONS

TECHNICAL REPORTS: Scientific and technical information considered important, complete, and a lasting contribution to existing knowledge.

TECHNICAL NOTES: Information less broad in scope but nevertheless of importance as a contribution to existing knowledge.

TECHNICAL MEMORANDUMS: Information receiving limited distribution because of preliminary data, security classification, or other reasons.

CONTRACTOR REPORTS: Technical information generated in connection with a NASA contract or grant and released under NASA auspices.

TECHNICAL TRANSLATIONS: Information published in a foreign language considered to merit NASA distribution in English.

TECHNICAL REPRINTS: Information derived from NASA activities and initially published in the form of journal articles.

SPECIAL PUBLICATIONS: Information derived from or of value to NASA activities but not necessarily reporting the results of individual NASA-programmed scientific efforts. Publications include conference proceedings, monographs, data compilations, handbooks, sourcebooks, and special bibliographies.

Details on the availability of these publications may be obtained from:

SCIENTIFIC AND TECHNICAL INFORMATION DIVISION

NATIONAL AERONAUTICS AND SPACE ADMINISTRATION

Washington, D.C. 20546